nature portfolio

https://doi.org/10.1038/s41929-021-00578-1

Supplementary information

Redirecting dynamic surface restructuring of a layered transition metal oxide catalyst for superior water oxidation

In the format provided by the authors and unedited

Supplementary information

Redirecting Dynamic Surface Restructuring of a Layered Transition Metal Oxide Catalyst for Superior Water Oxidation

Contents:

Supplementary Figures

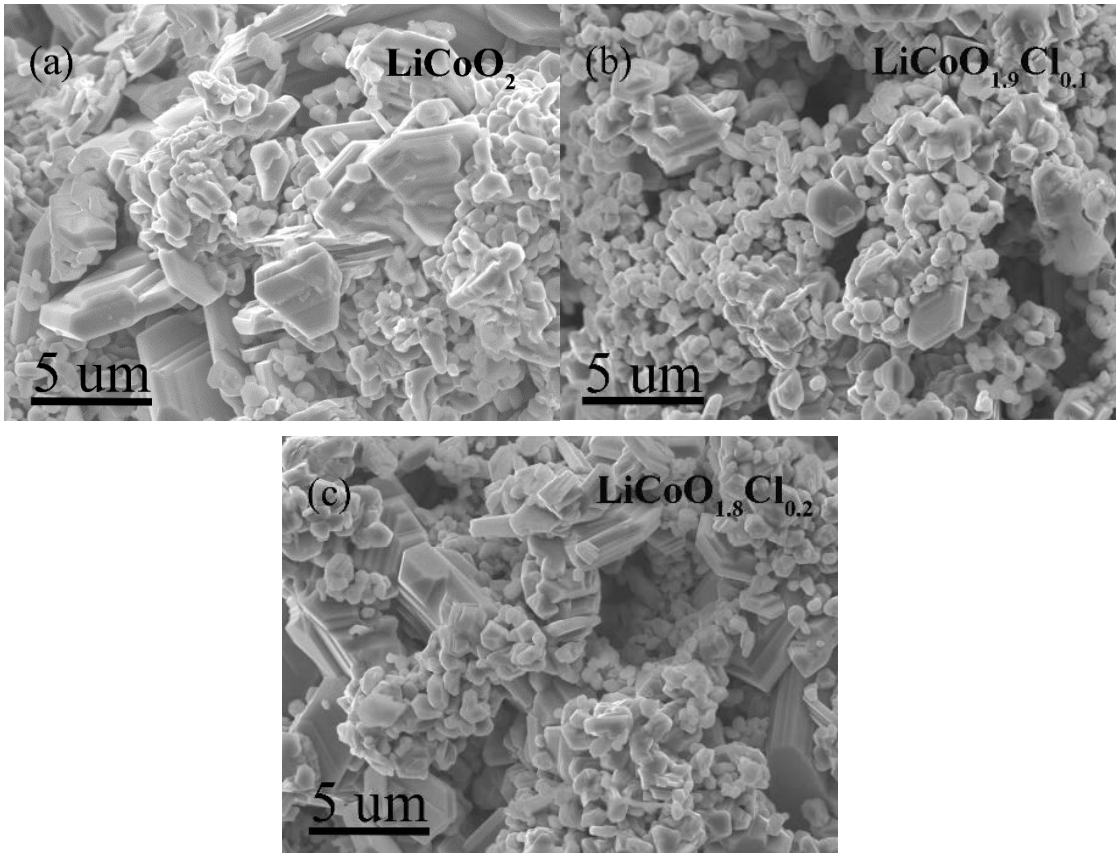

Supplementary Figure 1: SEM image of **(a)** $LiCoO_2$; **(b)** $LiCoO_{1.9}Cl_{0.1}$; **(c)** $LiCoO_{1.8}Cl_{0.2}$.

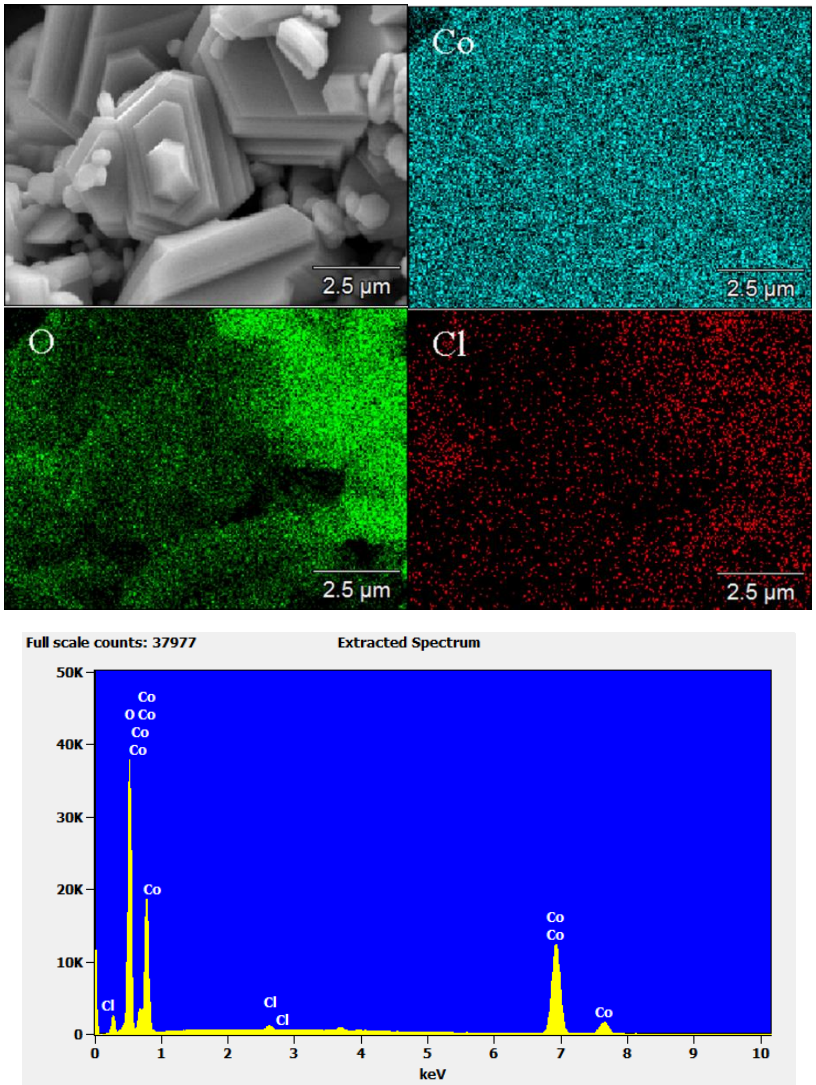

Supplementary Figure 2: SEM image, corresponding EDS mapping, and EDS spectrum for $LiCoO_{1.8}Cl_{0.2}$.

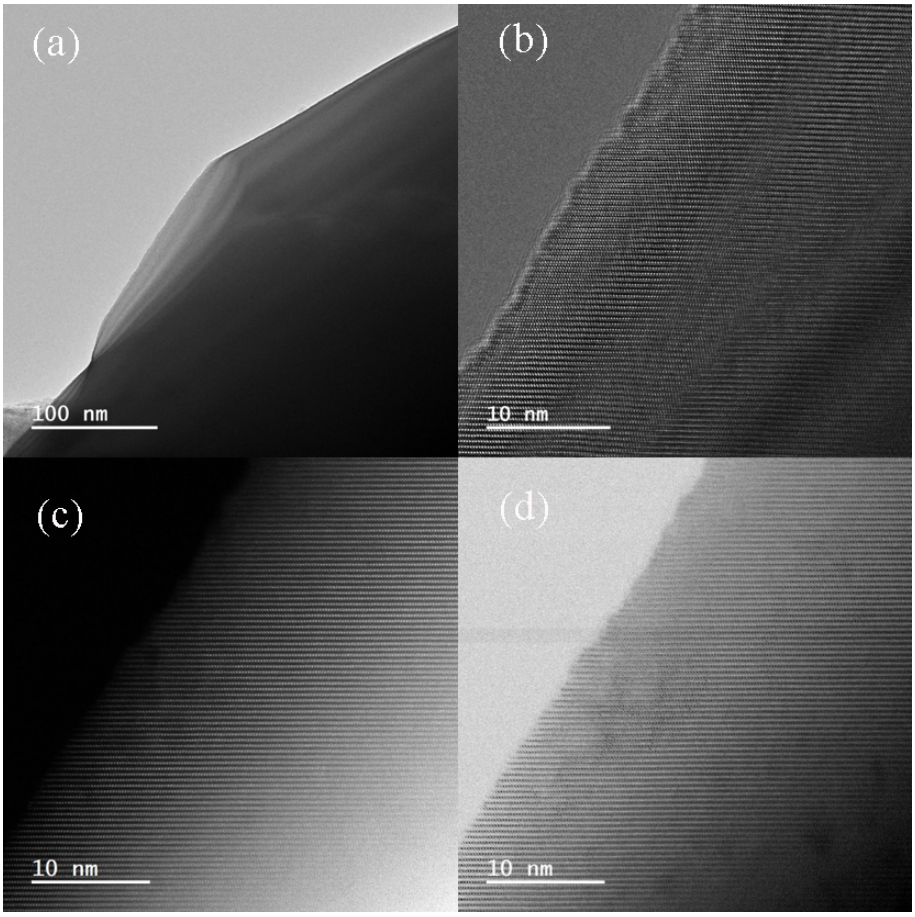

Supplementary Figure 3: Structural characterization of $LiCoO_{1.8}Cl_{0.2}$: **(a)** TEM; **(b)** Cs-HRTEM; **(c)** HAADF-STEM; and **(d)** BF-STEM.

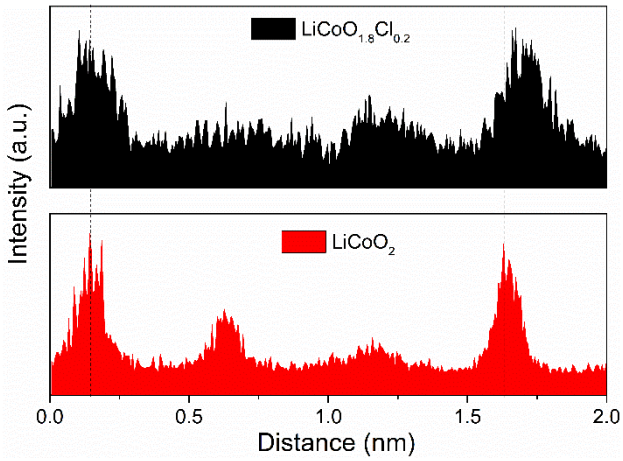

Supplementary Figure 4: Intensity line profile of the cobalt column extracted along the c-axis direction in Figure 1(a) and (b) in the main text, where the peaks and valleys represent Co atoms and gaps, respectively.

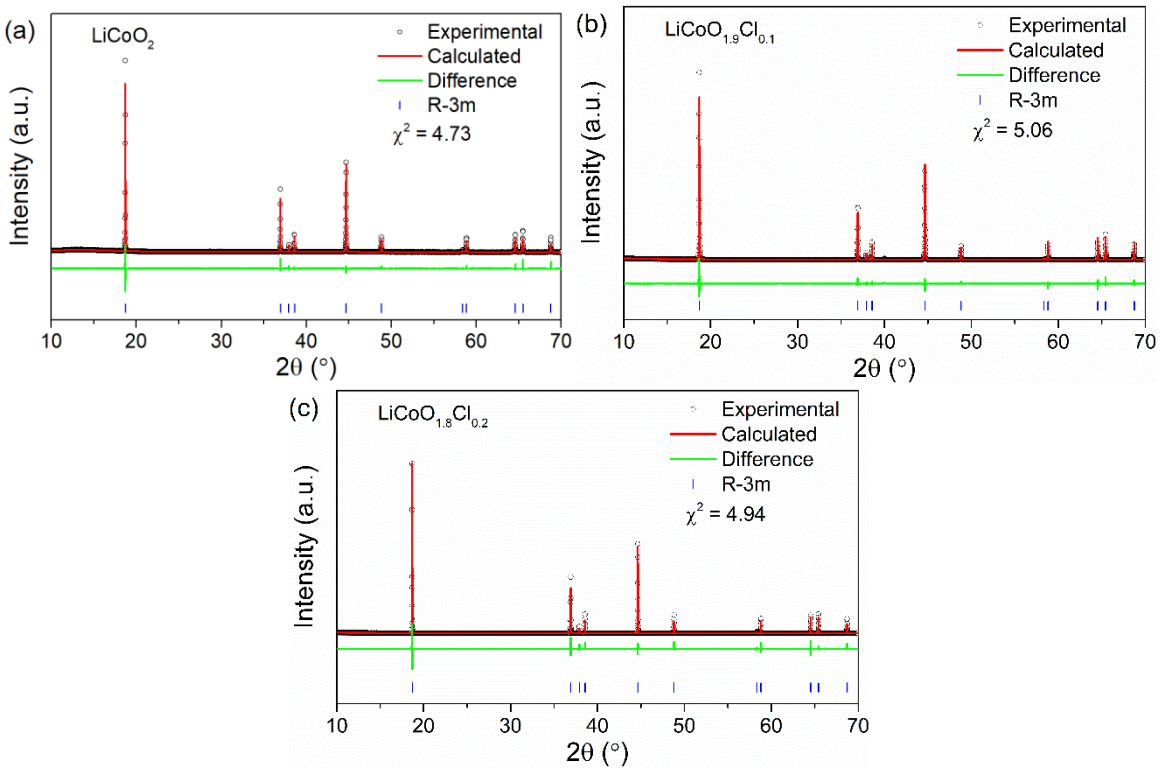

Supplementary Figure 5: XRD Rietveld refinement for **(a)** $LiCoO_2$; **(b)** $LiCoO_{1.9}Cl_{0.1}$; **(c)** $LiCoO_{1.8}Cl_{0.2}$.

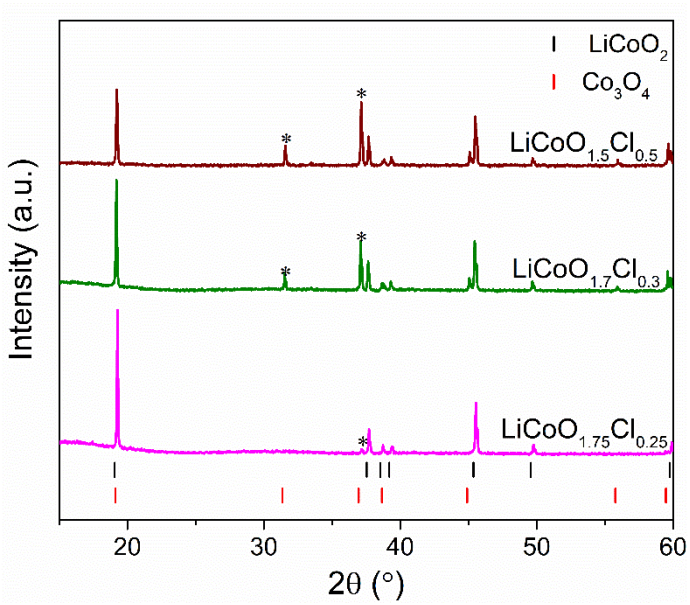

Supplementary Figure 6: XRD patterns of $LiCoO_2$ doped with different Cl levels, where * marks the impure phases.

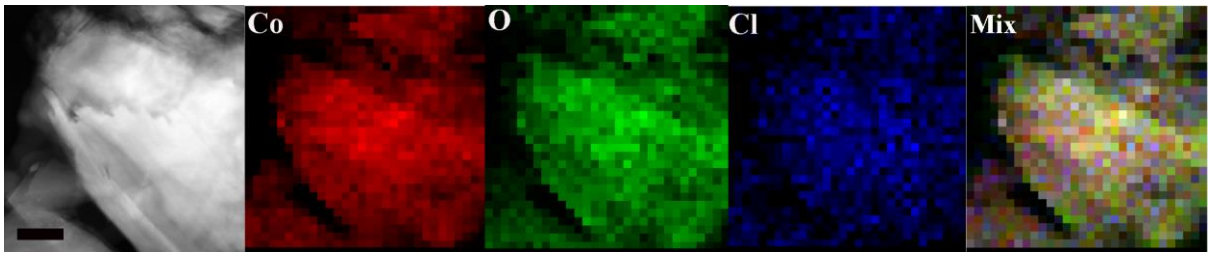

Supplementary Figure 7: STEM image of $LiCoO_{1.8}Cl_{0.2}$ and corresponding elemental EDS mapping of Co, O, Cl, and their overlap. Scale bar: 100 nm.

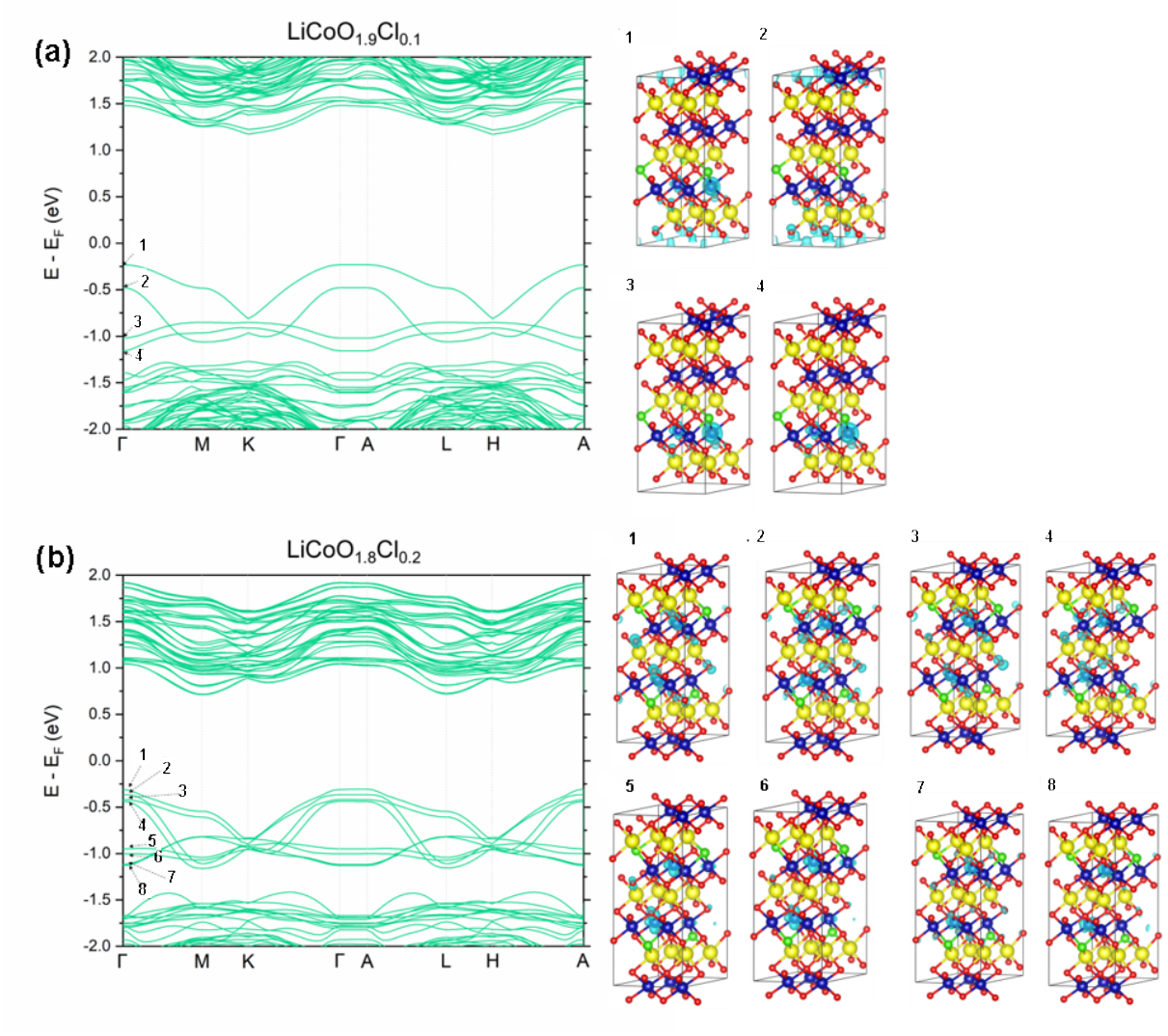

Supplementary Figure 8: Electronic band structures and band-decomposed charge density distributions of **(a)** $LiCoO_{1.9}Cl_{0.1}$; **(b)** $LiCoO_{1.8}Cl_{0.2}$.

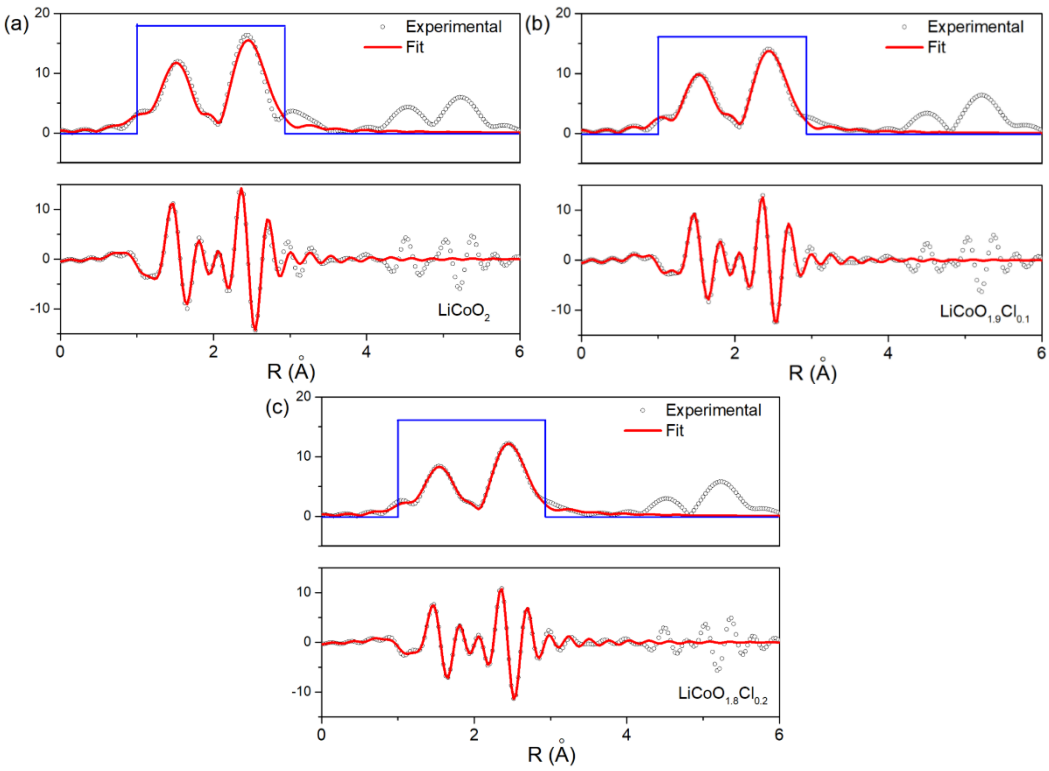

Supplementary Figure 9: Fitting of Fourier transformed k^3 -weighted Co K edge EXAFS recorded for **(a)** $LiCoO_2$; **(b)** $LiCoO_{1.9}Cl_{0.1}$; **(c)** $LiCoO_{1.8}Cl_{0.2}$.The fitting was conduceted within the range of 1 - 2.9 Å. The amplitude reduction factor S_0^2 was determined by fitting $LiCoO_2$. The theoretic model for the structure of $LiCoO_2$, $LiCoO_{1.9}Cl_{0.1}$, and $LiCoO_{1.8}Cl_{0.2}$ were obtained from the Rietveld refinement results of synchrotron-based XRD in Supplementary Tables 2-4.

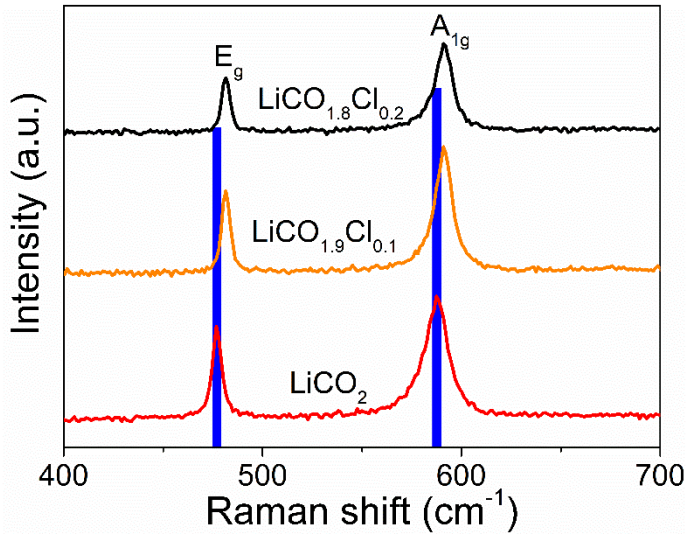

Supplementary Figure 10: Raman spectrum of $LiCoO_2$, $LiCoO_{1.9}Cl_{0.1}$, and $LiCoO_{1.8}Cl_{0.2}$. Two characteristic peaks around 590 cm^{-1} and 480 cm^{-1} were detected, corresponding to the Co-O A_{1g} stretching mode and O-Co-O E_g bending mode. In comparison to pristine $LiCO_2$, the Raman scattering mode of Cl-doped LCO is shifted towards high wave number, concurring with their reduced Co valence state.[1]

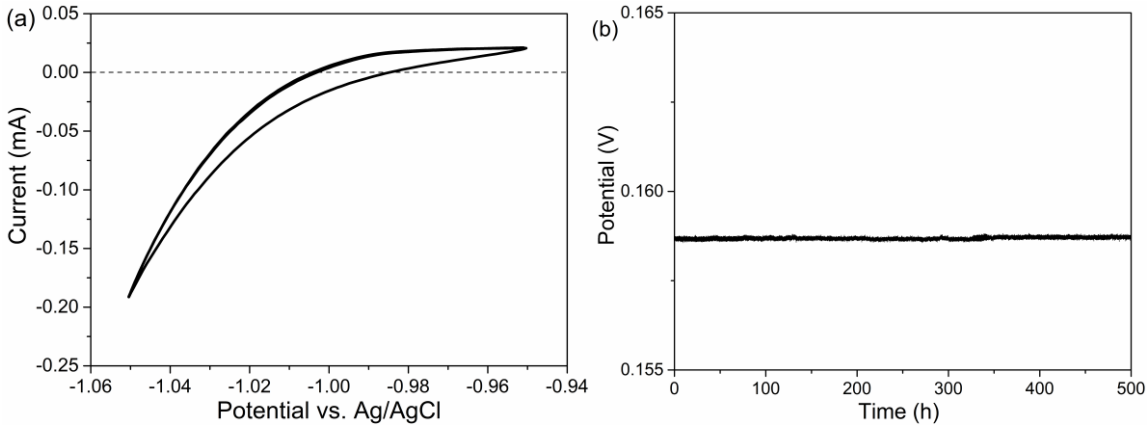

Supplementary Figure 11: **(a)** RHE correction of Ag/AgCl reference electrode in 1 M KOH, with Pt foil, Pt wire, and Ag/AgCl serving as the working, counter, and reference electrode, respectively. The CV scanning rate was equal to 1 mV s^{-1}. **(b)** The potential difference between Ag/AgCl and Hg/HgO (ALS) in 1M KOH.

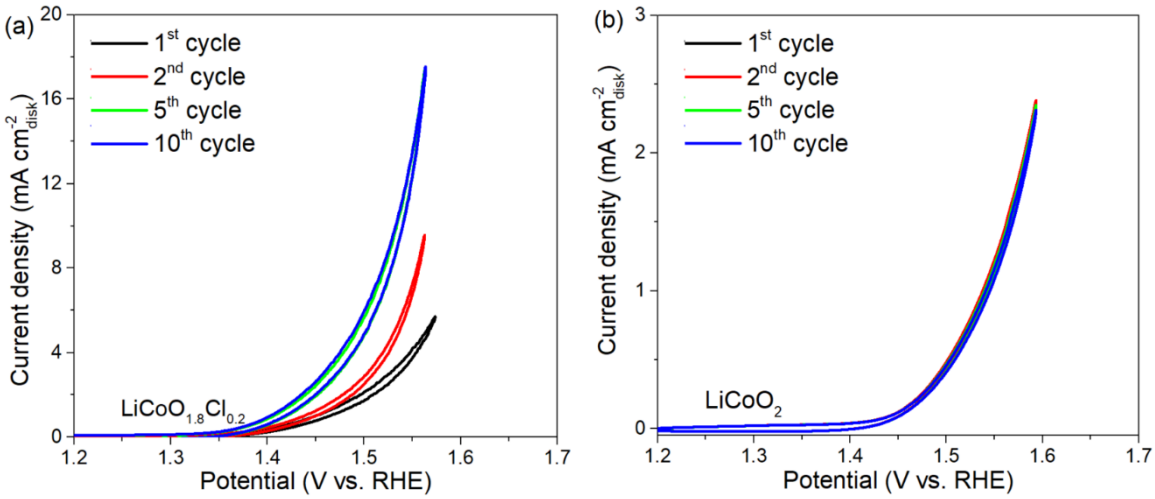

Supplementary Figure 12: CV scans in the potential region of 1.2 - 1.6 V vs. RHE for **(a)** $LiCoO_{1.8}Cl_{0.2}$ and **(b)** $LiCoO_2$.

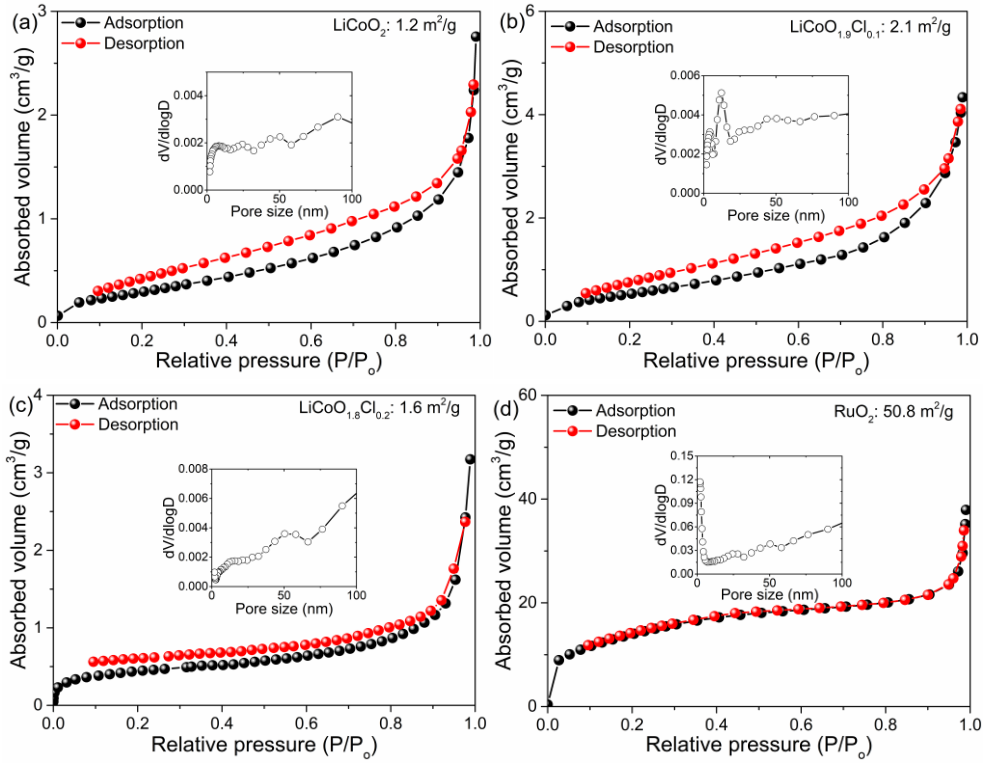

Supplementary Figure 13: N_2 adsorption-desorption isotherm curves. **(a)** $LiCoO_2$; **(b)** $LiCoO_{1.9}Cl_{0.1}$; **(c)** $LiCoO_{1.8}Cl_{0.2}$; **(d)** RuO_2. Each inset plot depicts the corresponding Barrett-Joyner-Halenda (BJH) pore size distribution.

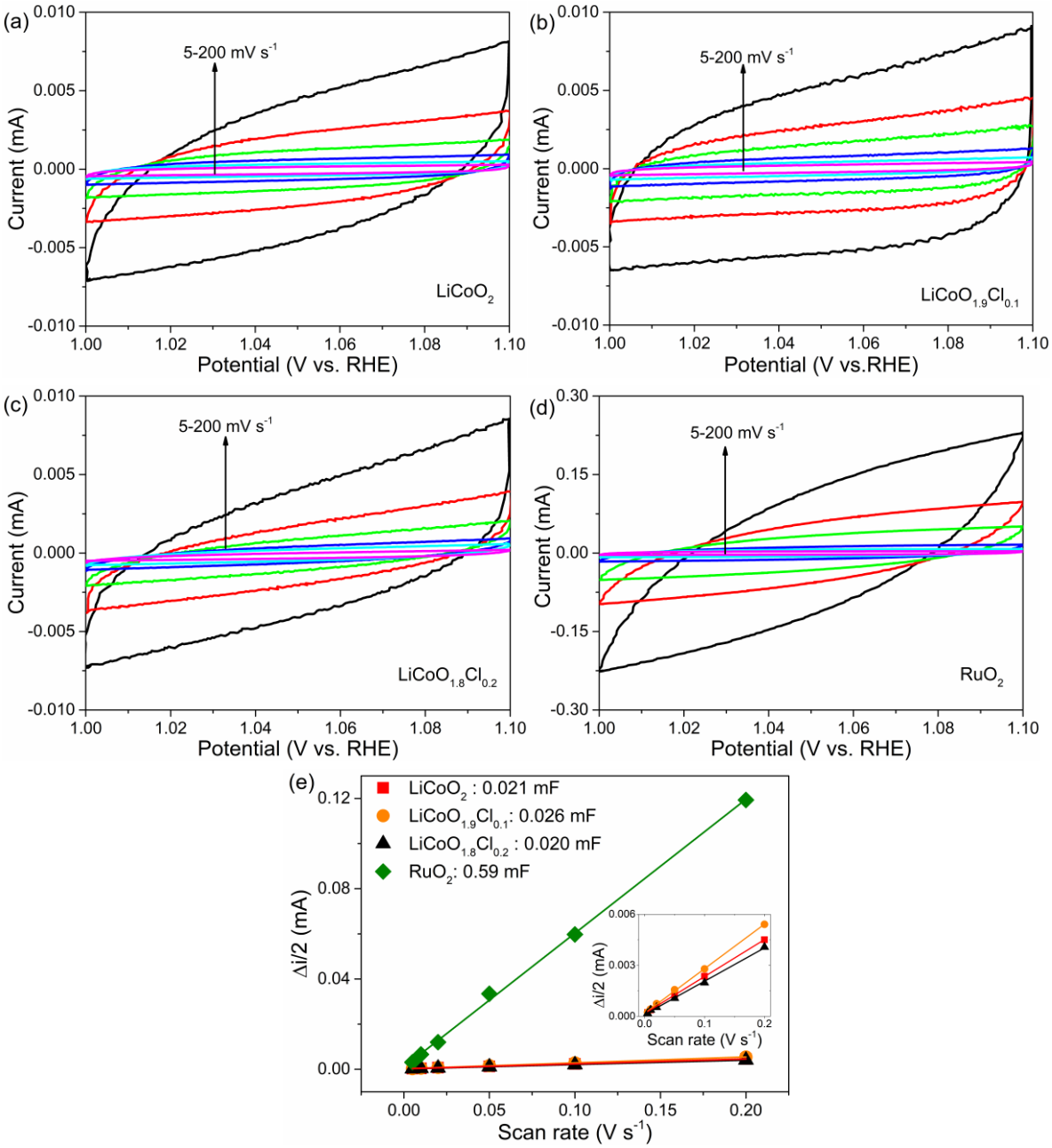

Supplementary Figure 14: CV curves in the potential region of 1-1.1 V vs. RHE for **(a)** $LiCoO_2$; **(b)** $LiCoO_{1.9}Cl_{0.1}$; **(c)** $LiCoO_{1.8}Cl_{0.2}$; and **(d)** RuO_2. **(e)** The dependence of the capacitive current on the different potential scan rates. The inset is a magnified plot for $LiCoO_2$, $LiCoO_{1.9}Cl_{0.1}$, and $LiCoO_{1.8}Cl_{0.2}$.

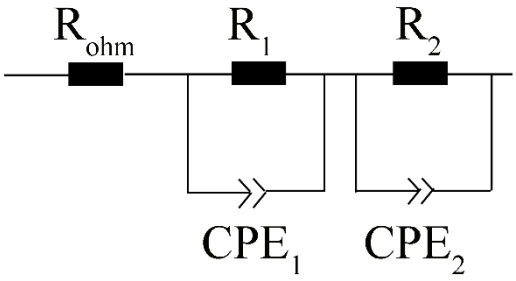

Supplementary Figure 15: Equivalent circuit used for the fitting of the EIS responses, where R_{ohm}, R_1, R_2, CPE_1, and CPE_2 represent the solution resistance, electrode texture and charge transfer resistances, and constant phase elements, respectively.[2,3]

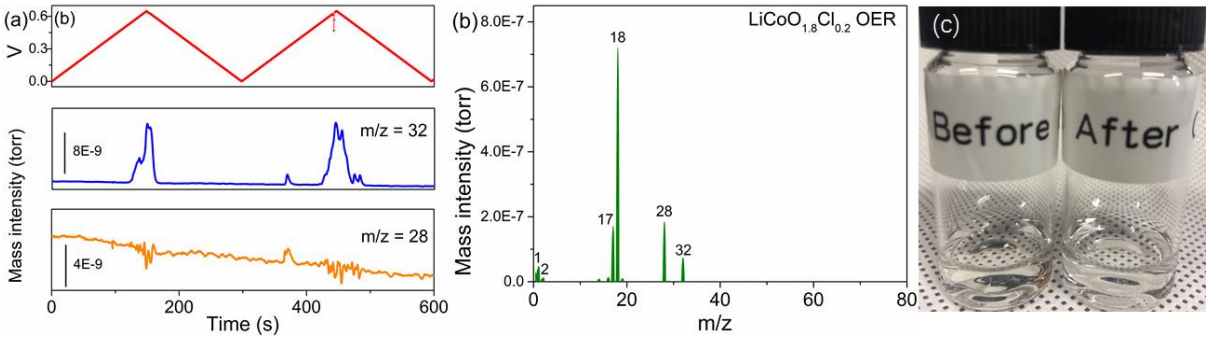

Supplementary Figure 16: DEMS experiment for $LiCoO_{1.8}Cl_{0.2}$/glassy carbon electrode in 1 M KOH: **(a)** selected gases profile within two CV cycles (0-0.7 V vs. Ag/AgCl); **(b)** Gas profile at 0.7 V vs. Ag/AgCl. **(c)** Photo of the electrolyte solution (1 M KOH) titrated by $AgNO_3$ aqueous solution with excessive HNO_3 before and after cycling $LiCoO_{1.8}Cl_{0.2}$ for 1000 cycles.

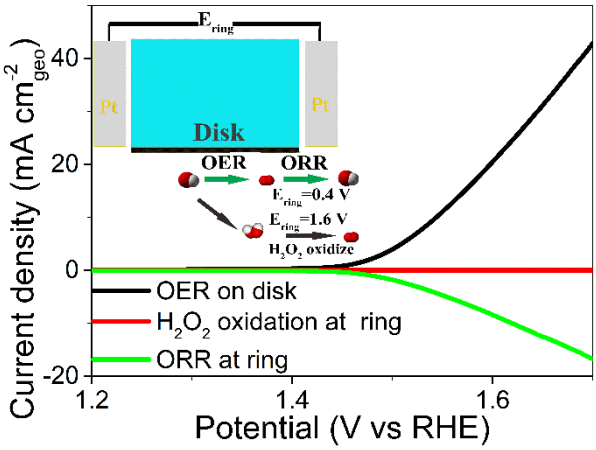

Supplementary Figure 17: RRDE setup to detect ORR current (V_{ring} = 0.4 V vs. RHE) or potentially generated H_2O_2 (V_{ring} = 1.5 V vs. RHE) on the Pt ring during the $LiCoO_{1.8}Cl_{0.2}$ catalysis on the disk.

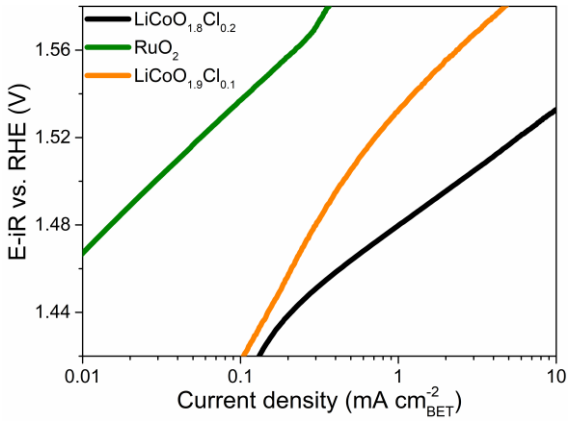

Supplementary Figure 18: Specific OER activity normalized by the BET surface area.

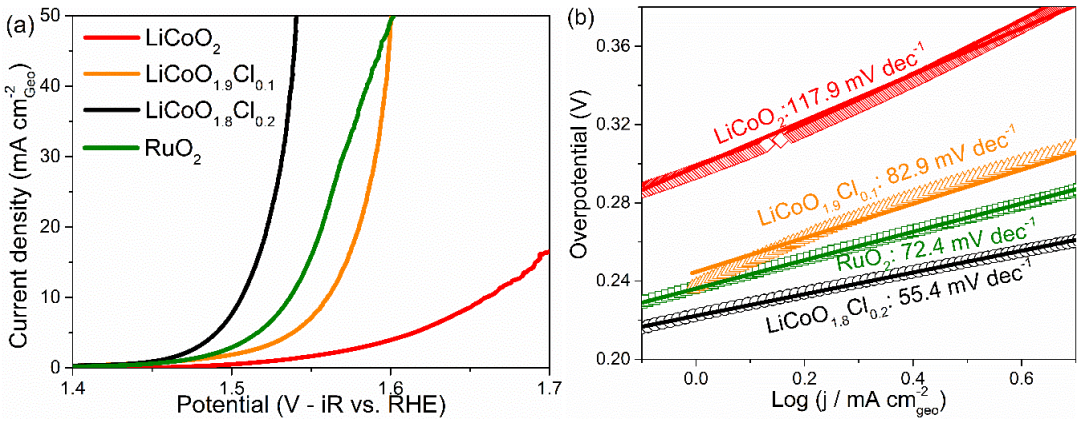

Supplementary Figure S19: OER geometric activity normalized by glassy carbon disk area :

(a) LSV; (b) Tafel plot.

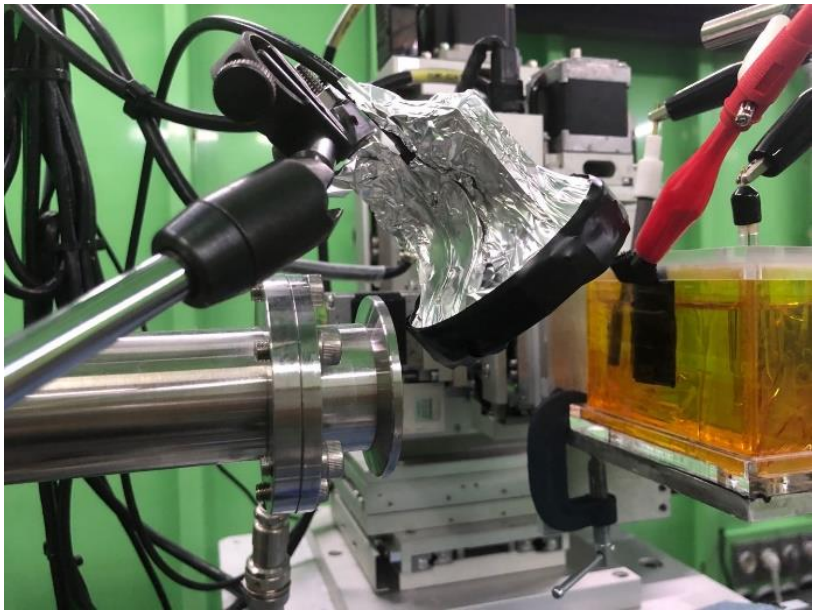

Supplementary Figure 20: Photo of the setup for the operando X-ray absorption spectroscopy test. The Operando XAS tests were conducted with the homemade cell, where the investigated catalysts were loaded on the carbon cloth serving as the working electrode. Graphite rod and Ag/AgCl filled with 3 M NaCl performed as the counter and reference electrode, respectively. The backside of the carbon cloth was pasted by Kapton film to prevent the electrolyte from leakage and to allow the X-rays to transmit. XAS spectra were collected with the fluorescence mode.[4] The XANES and EXAFS were collected during the chronoamperometry measurement, where the working potential was held at 1.2, 1.4, 1.5, 1.6 V vs. RHE and ceased, respectively.

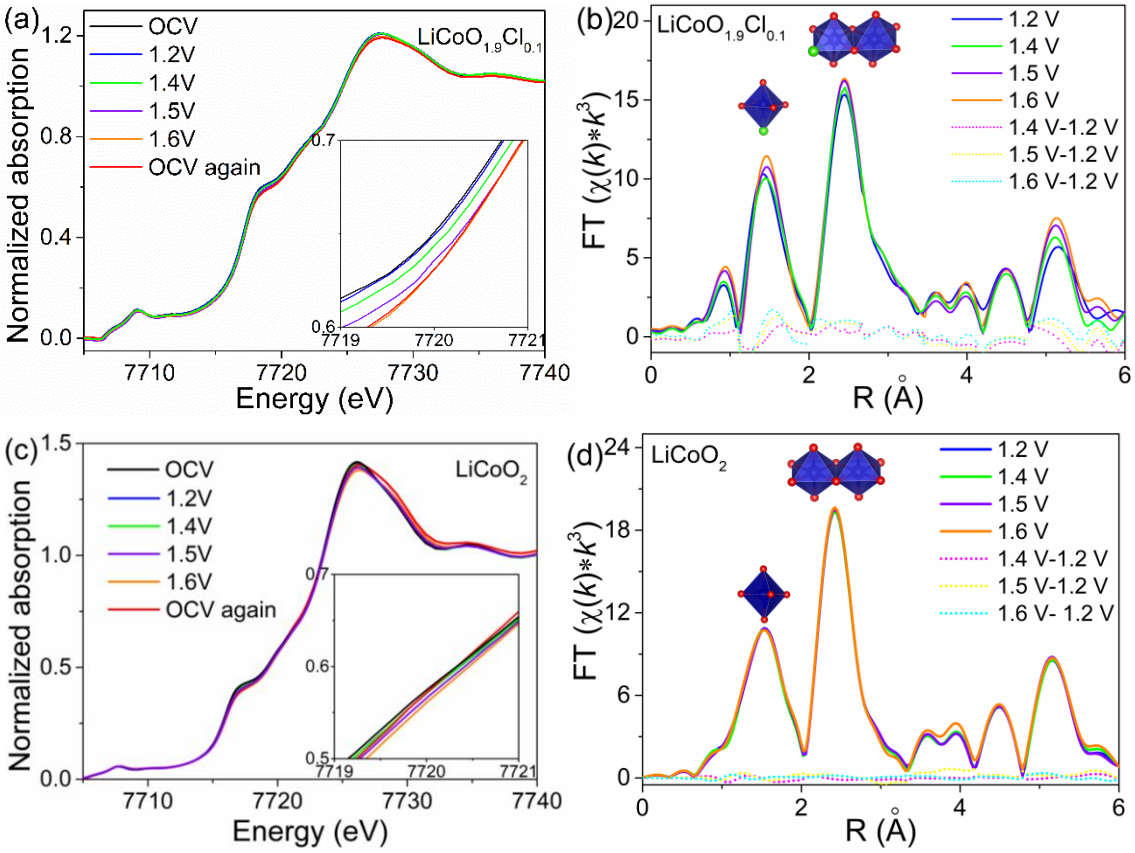

Supplementary Figure 21: Operando Co K-edge XANES spectra and EXAFS recorded at different potentials during OER for **(a)** and **(b)** fresh $LiCoO_{1.9}Cl_{0.1}$; **(c)** and **(d)** fresh $LiCoO_2$ without cycling.

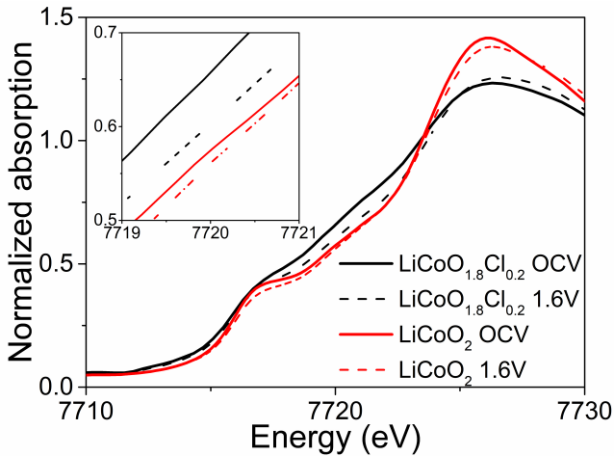

Supplementary Figure 22: Comparison of Co K-edge XANES spectra recorded at OCV and 1.6 V vs. RHE during the initial polarization.

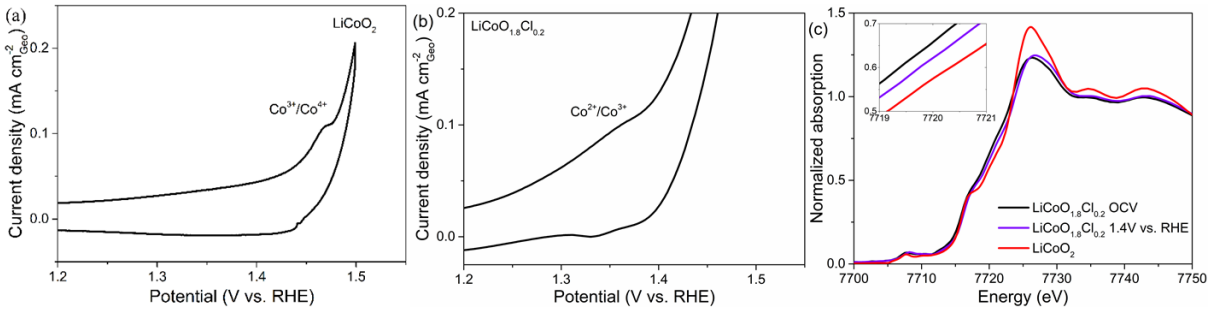

Supplementary Figure 23. The first CV scan for **(a)** $LiCoO_2$ and **(b)** $LiCoO_{1.8}Cl_{0.2}$, where the assignment of valence state change agrees with published literature: Co^{2+}/Co^{3+} redox takes place before 1.4 V vs. RHE, while Co^{3+}/Co^{4+} redox happens around 1.5 V vs. RHE.[5] **(c)** Normalized Co K-edge XANES spectra of pristine $LiCoO_{1.8}Cl_{0.2}$ ($LiCoO_{1.8}Cl_{0.2}$ OCV), cycled $LiCoO_{1.8}Cl_{0.2}$ to 1.4 V vs. RHE ($LiCoO_{1.8}Cl_{0.2}$ 1.4 V vs. RHE), and $LiCoO_2$ during the initial polarization. In comparison to pristine $LiCoO_{1.8}Cl_{0.2}$ (mixed Co^{2+}/Co^{3+}), the Co K-edge of $LiCoO_{1.8}Cl_{0.2}$ at 1.4 V vs. RHE moved to a higher energy region by 0.3 eV, suggesting increased Co valence state. In addition, the Co K-edge of the $LiCoO_{1.8}Cl_{0.2}$ at 1.4 V vs. RHE was still below that of pristine $LiCoO_2$ with Co^{3+}, supporting that the cobalt redox transition of $LiCoO_{1.8}Cl_{0.2}$ was confined within the Co^{2+}/Co^{3+} region.

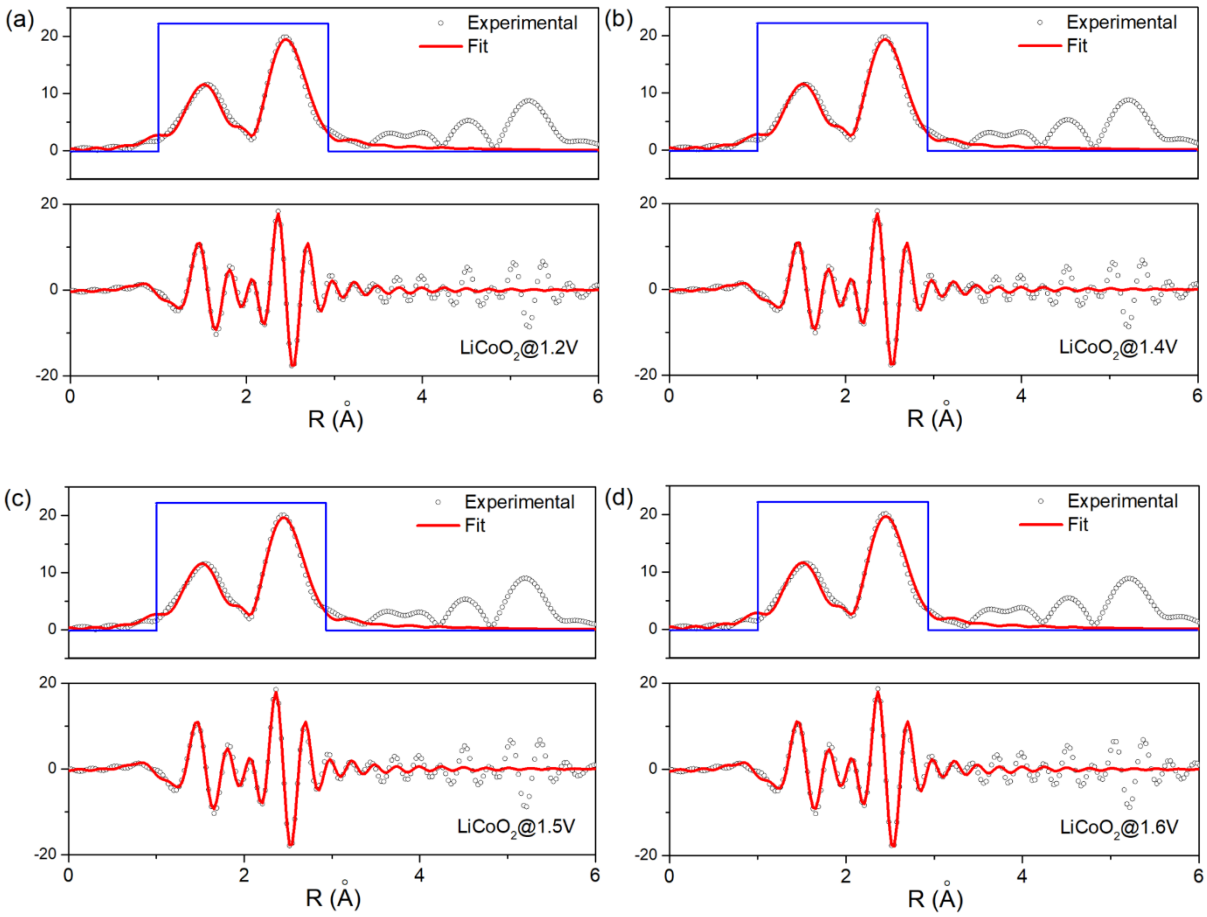

Supplementary Figure 24: Fitting of Fourier transformed k^3 -weighted Co K edge EXAFS recorded for $LiCoO_2$ at different OER potentials: **(a)** 1.2 V vs. RHE; **(b)** 1.4 V vs. RHE; **(c)** 1.5 V vs. RHE; **(d)** 1.6 V vs. RHE.

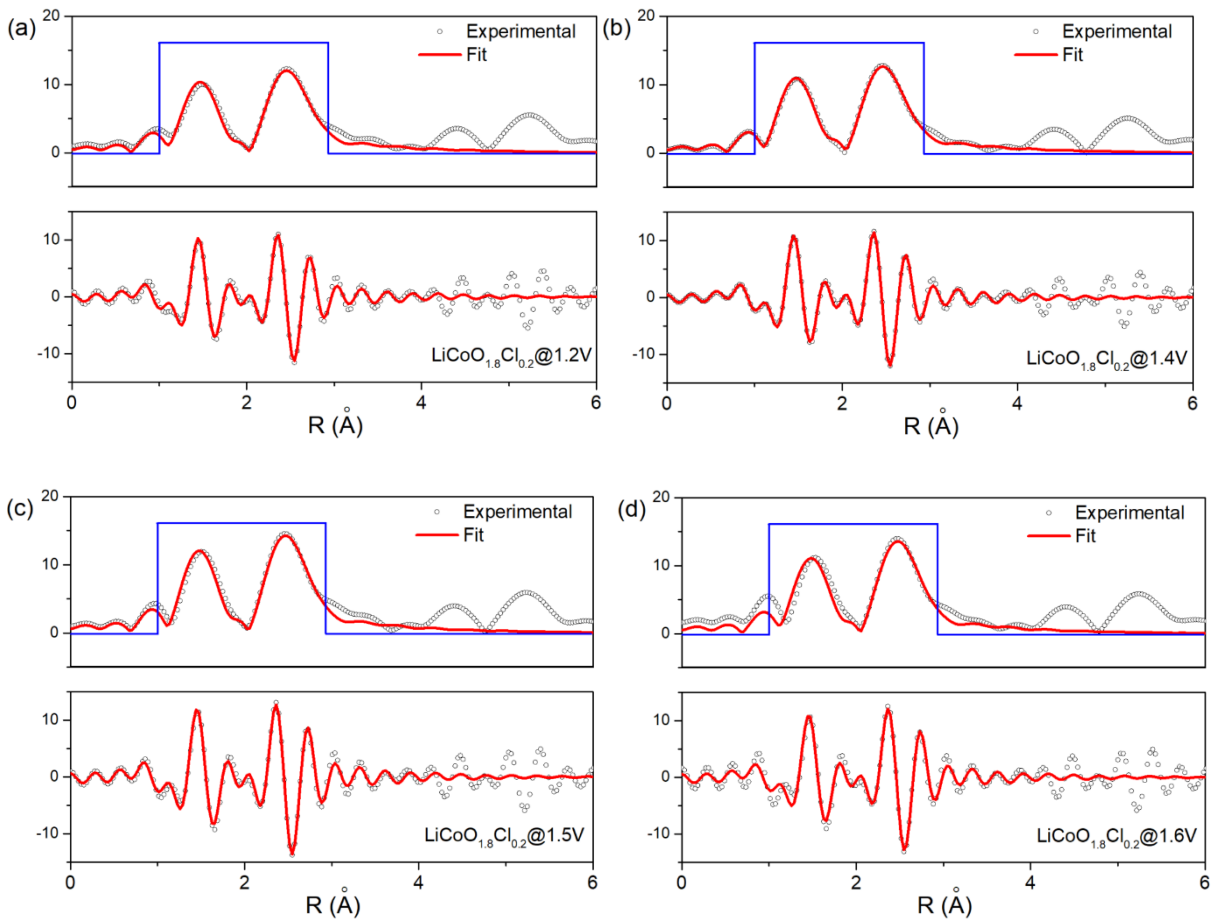

Supplementary Figure 25: Fitting of Fourier transformed k^3 -weighted Co K edge EXAFS recorded for $LiCoO_{1.8}Cl_{0.2}$ at different OER potentials: **(a)** 1.2 V vs. RHE; **(b)** 1.4 V vs. RHE; **(c)** 1.5 V vs. RHE; **(d)** 1.6 V vs. RHE.

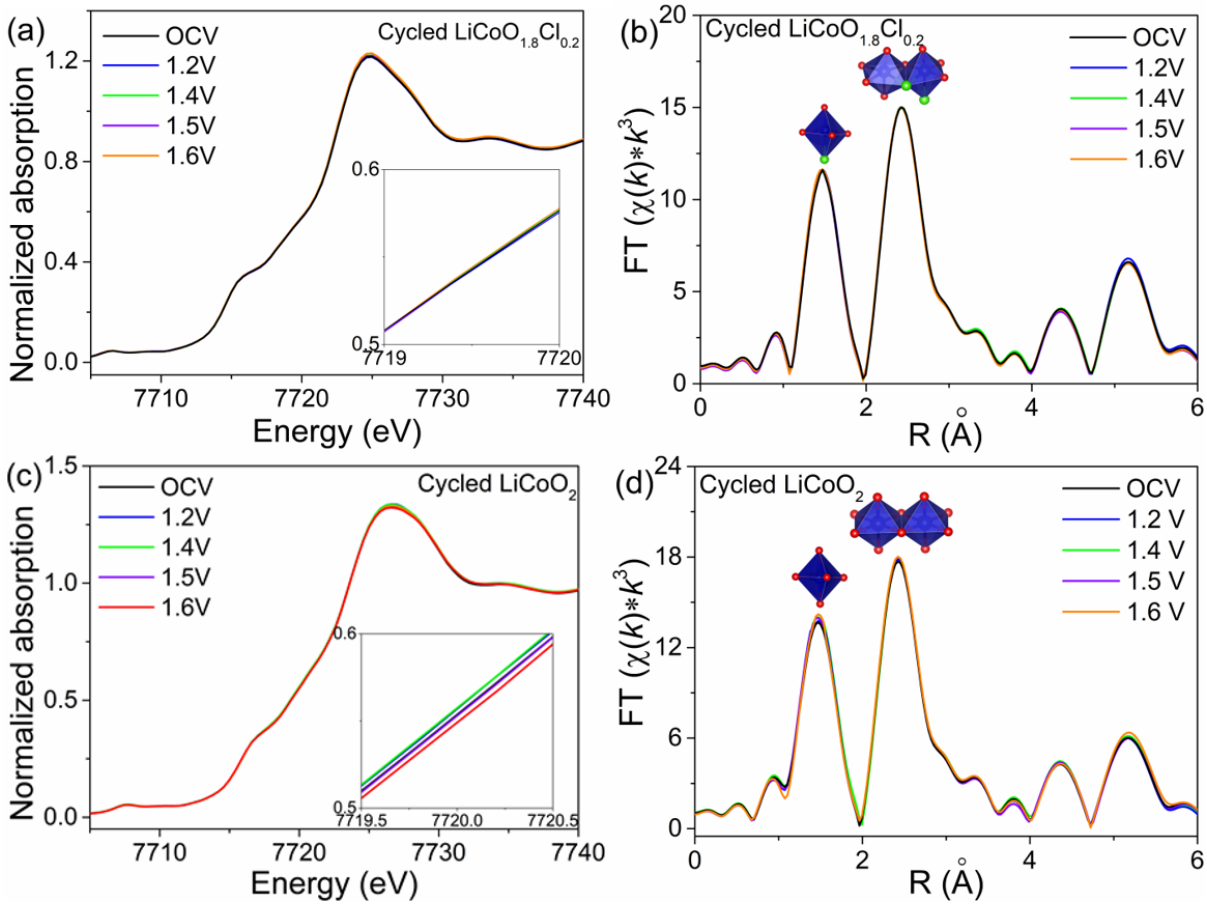

Supplementary Figure 26: Co K-edge XANES recorded at different potentials during OER after cycling **(a)** $LiCoO_{1.8}Cl_{0.2}$ and **(c)** $LiCoO_2$ OER potential regions for 20 cycles. Corresponding Fourier-transformed (FT) k^3-weighted Co K-edge EXAFS spectra: **(b)** $LiCoO_{1.8}Cl_{0.2}$; **(d)** $LiCoO_2$.

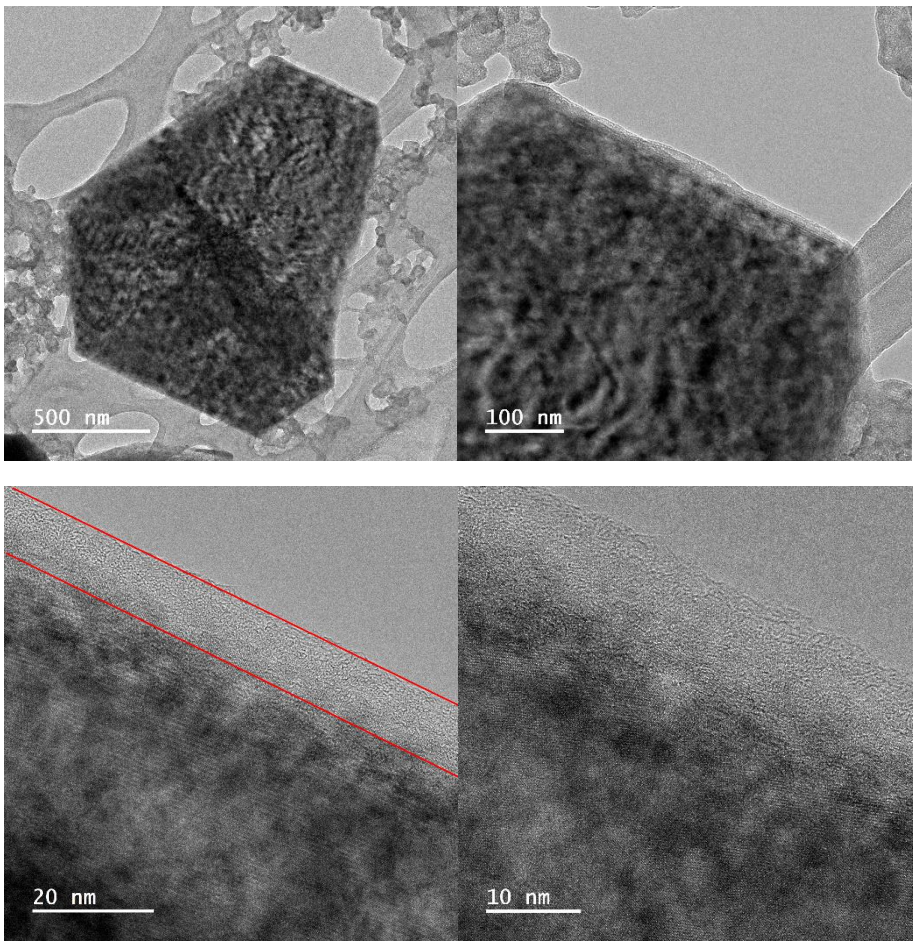

Supplementary Figure 27: Cs-TEM images of cycled $LiCoO_{1.8}Cl_{0.2}$ in OER potential regions for 20 cycles.

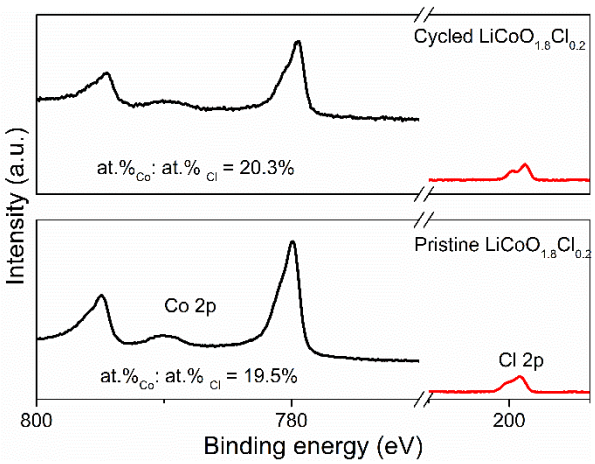

Supplementary Figure 28: Co 2p and Cl 2p XPS of pristine and cycled $LiCoO_{1.8}Cl_{0.2}$ between 1-1.6 V vs. RHE for 100 times.

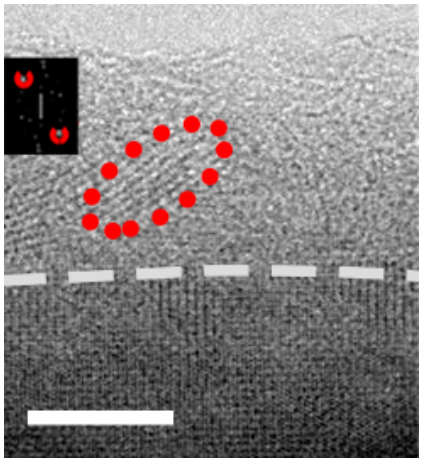

Supplementary Figure 29: BF-STEM image with the inset FFT for the circled region. Scale bar: 5 nm.

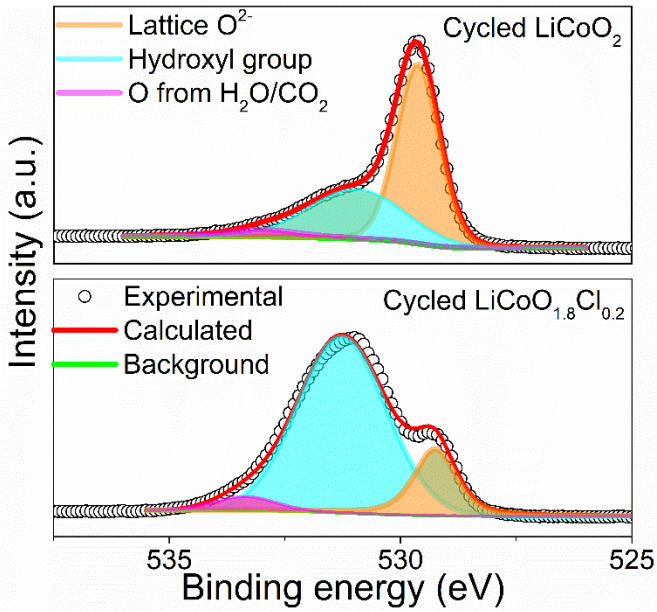

Supplementary Figure 30: O 2p XPS of cycled $LiCoO_{1.8}Cl_{0.2}$ and cycled $LiCoO_2$ between 1-1.6 V vs. RHE for 100 times.

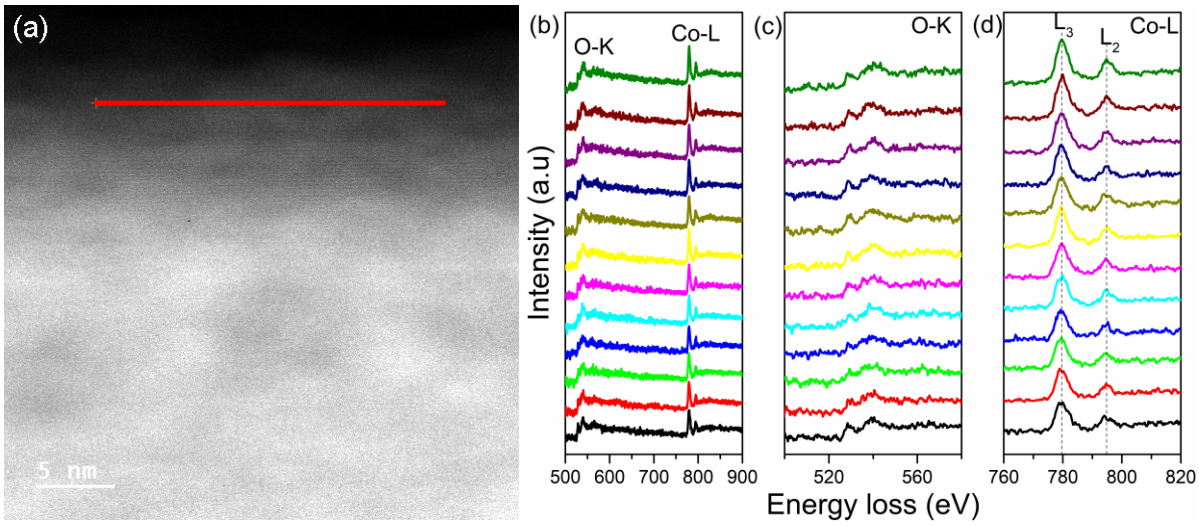

Supplementary Figure 31: STEM-EELS line scan across the surface of Cl-doped $LiCoO_2$ after cycling between 1 - 1.6 V vs. RHE for 20 cycles: **(a)** HAADF-STEM image of the region of interest, where the red line indicates the line scan pathways; **(b)** EELS line scan along the beam path indicated in **(a)**: the bottom (black) and top (olive) line correspond to the far left and right point in **(a)**; Individual EELS of **(c)** O K-edge and **(d)** Co L-edge.

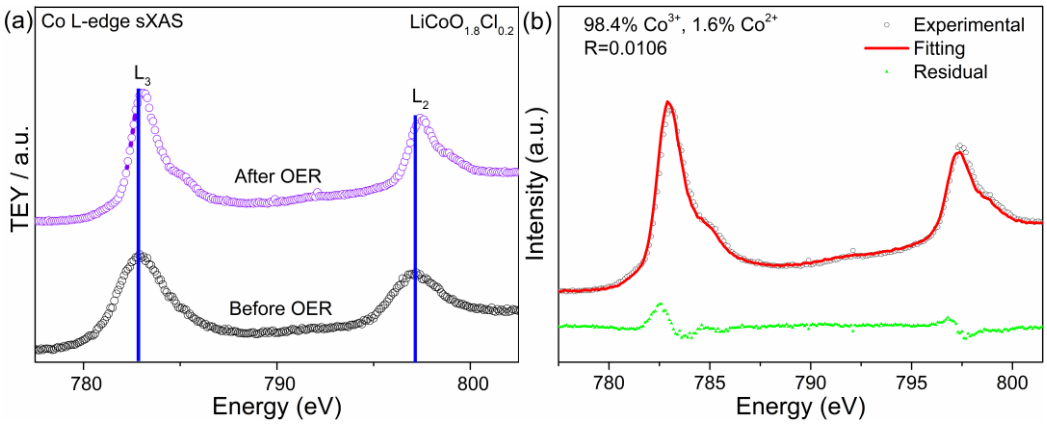

Supplementary Figure 32: **(a)** Co L-edge sXAS for cycled $LiCoO_{1.8}Cl_{0.2}$ and **(b)** the Linear combination fitting of cycled $LiCoO_{1.8}Cl_{0.2}$ with CoO and $LiCoO_2$ as the standard materials.

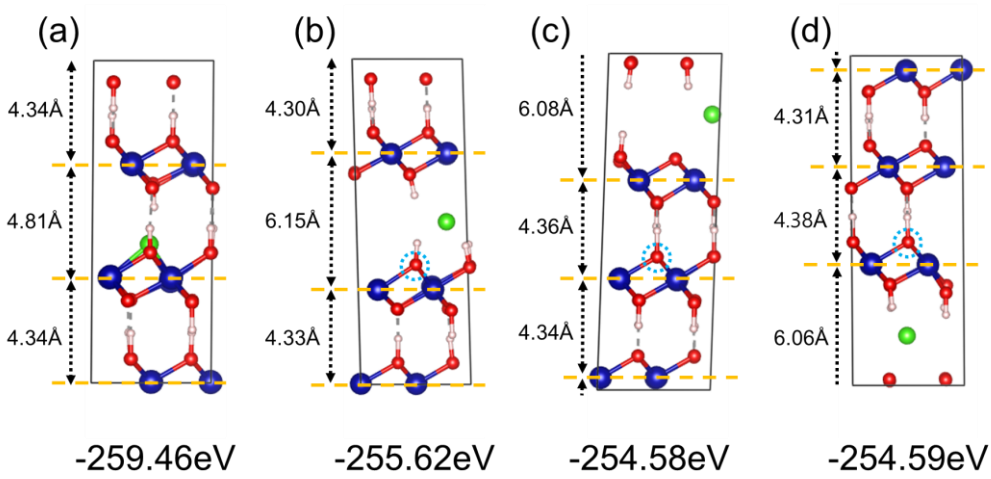

Supplementary Figure 33: DFT-optimized structures with **(a)** intralayer Cl^- ion and **(b-d)** interlayer Cl^- ion located at different interlayer locations. DFT total energy of each structure is also shown for energetic comparison. Dashed-cyan circle represents the O-vacant site. Cl, Co, O and H atoms are colored with green, blue, red and white, respectively. All considered structures with interlayer Cl^- were considerably unstable compared to the structure with intralayer Cl^- by 3.8-4.9 eV. Furthermore, the interlayer spacing was substantially increased to around 6.1 Å when Cl^- was located in between the layers, which supports that the large Cl^- cannot be accommodated in between the layers.

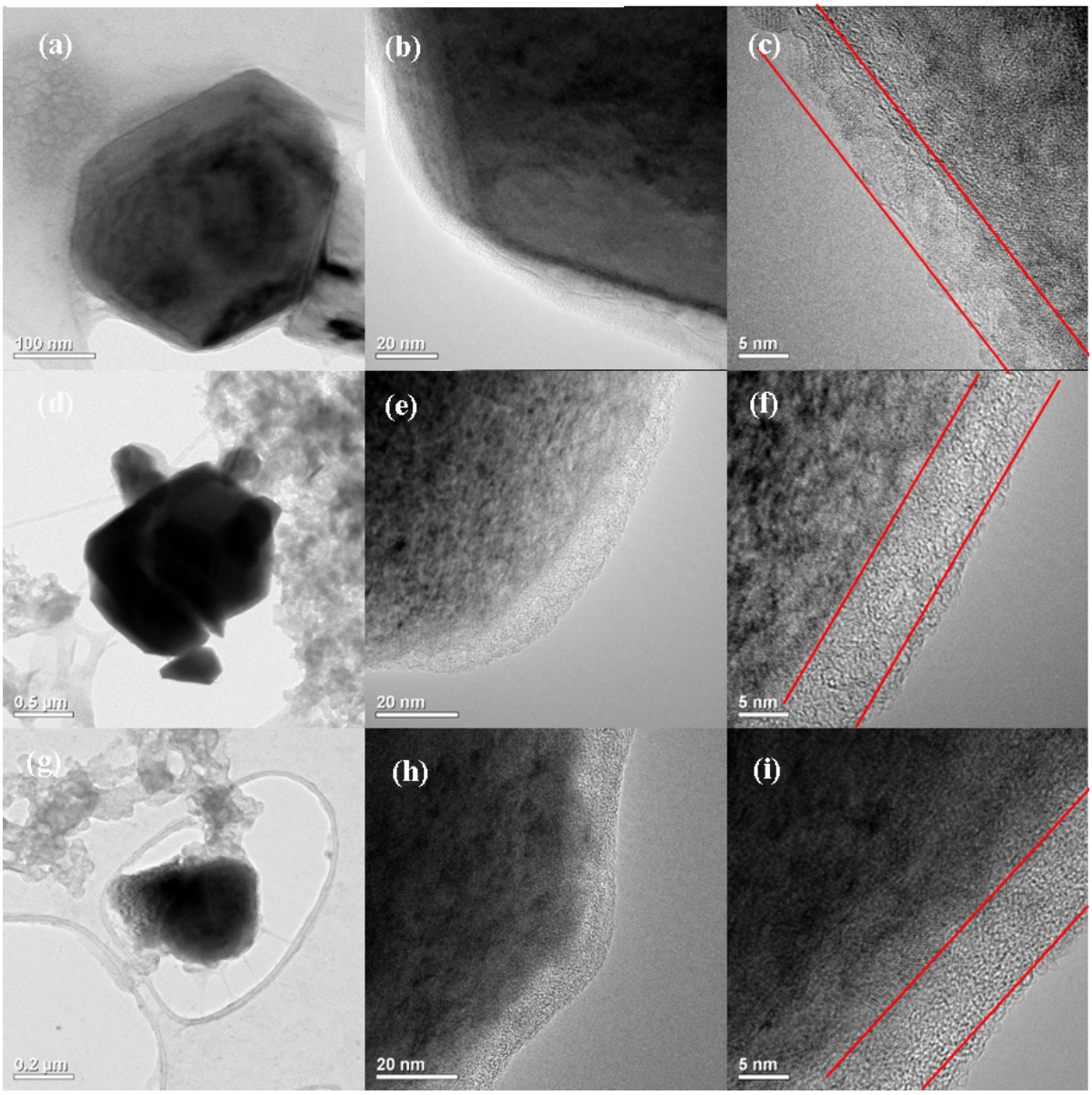

Supplementary Figure 34: TEM images of $LiCoO_{1.8}Cl_{0.2}$ after cycling in OER potential regions for **(a)-(c)** 30 cycles; **(d)-(f)** 350 cycles; **(g)-(i)** 1000 cycles.

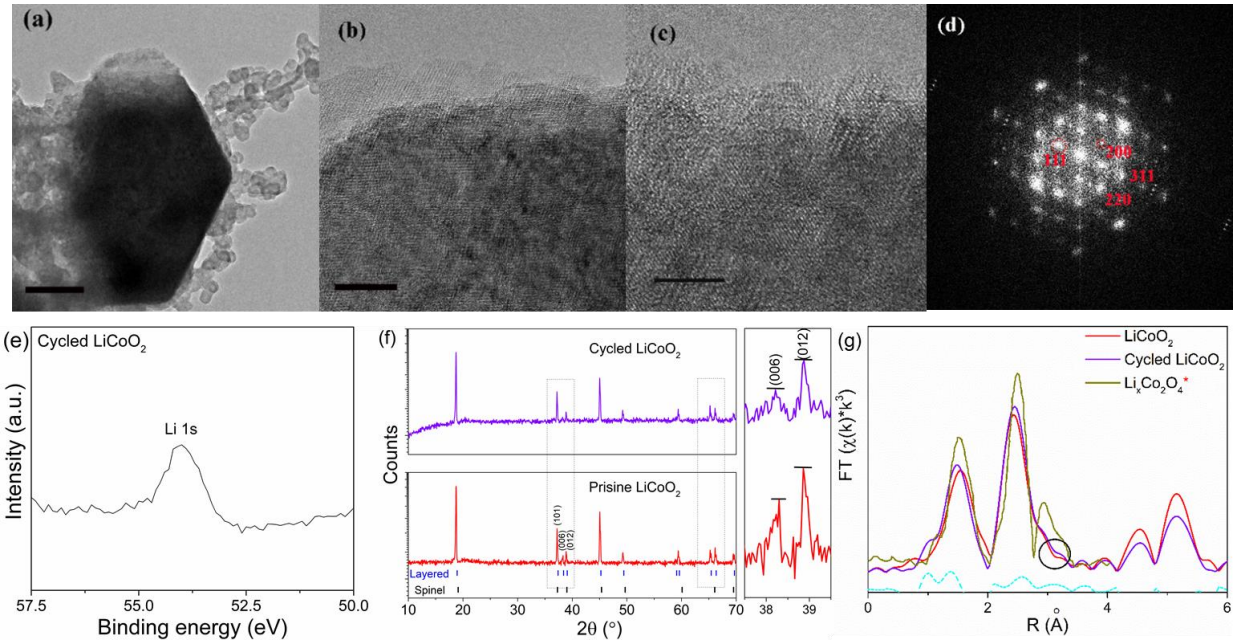

Supplementary Figure 35: Structural and compositional characterization of cycled $LiCoO_2$ between 1 - 1.6 V vs. RHE for 100 cycles: **(a)** TEM, **(b)** and **(c)** Cs-HRTEM image, **(d)** FFT of **(c)**, Where the scale bar in **(a)**, **(b)** and **(c)** represent 250, 10, and 5 nm, respectively. **(e)** Li 1s XPS. **(f)** XRD. **(g)** Co K-edge k^3-weighted EXAFS, where * is extracted from the reference.[6]

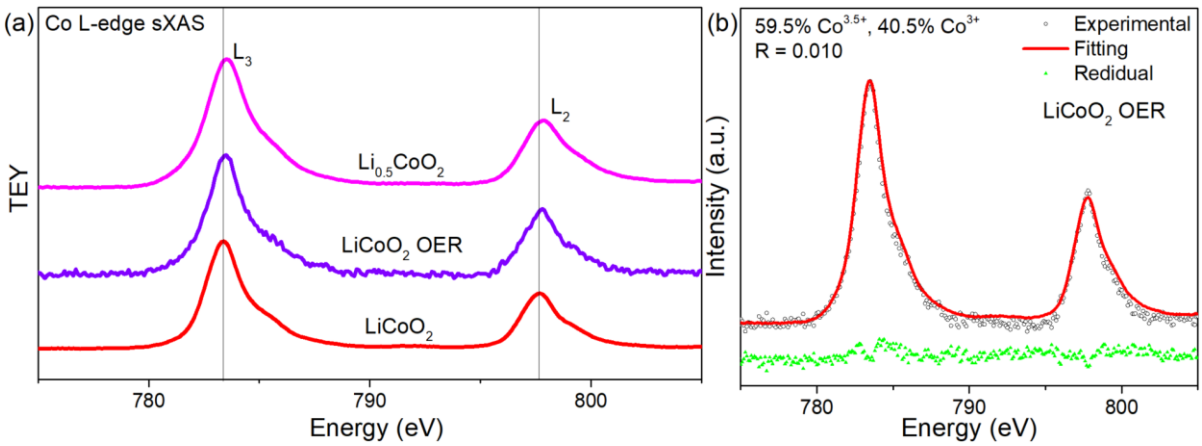

Supplementary Figure 36: (a) Co L-edge TEY sXAS of pristine $LiCoO_2$, $LiCoO_2$ OER (cycled within 1 -1.6 V vs. RHE for 100 cycles), and chemical delithiation-derived $Li_{0.5}CoO_2$. In comparison to pristine $LiCoO_2$, the Co $L_{2,3}$ edge of cycled $LiCoO_2$ ($LiCoO_2$ OER) shifted toward the higher energy regions by ~ 0.1 eV, suggesting that the valence state of its surface Co was higher than that of +3. **(b)** Fitting of Co L-edge soft XAS for cycled $LiCoO_2$ by using $LiCoO_2$ (Co^{3+}) and chemical delithiation-derived $Li_{0.5}CoO_2$ ($Co^{3.5+}$) as the references.

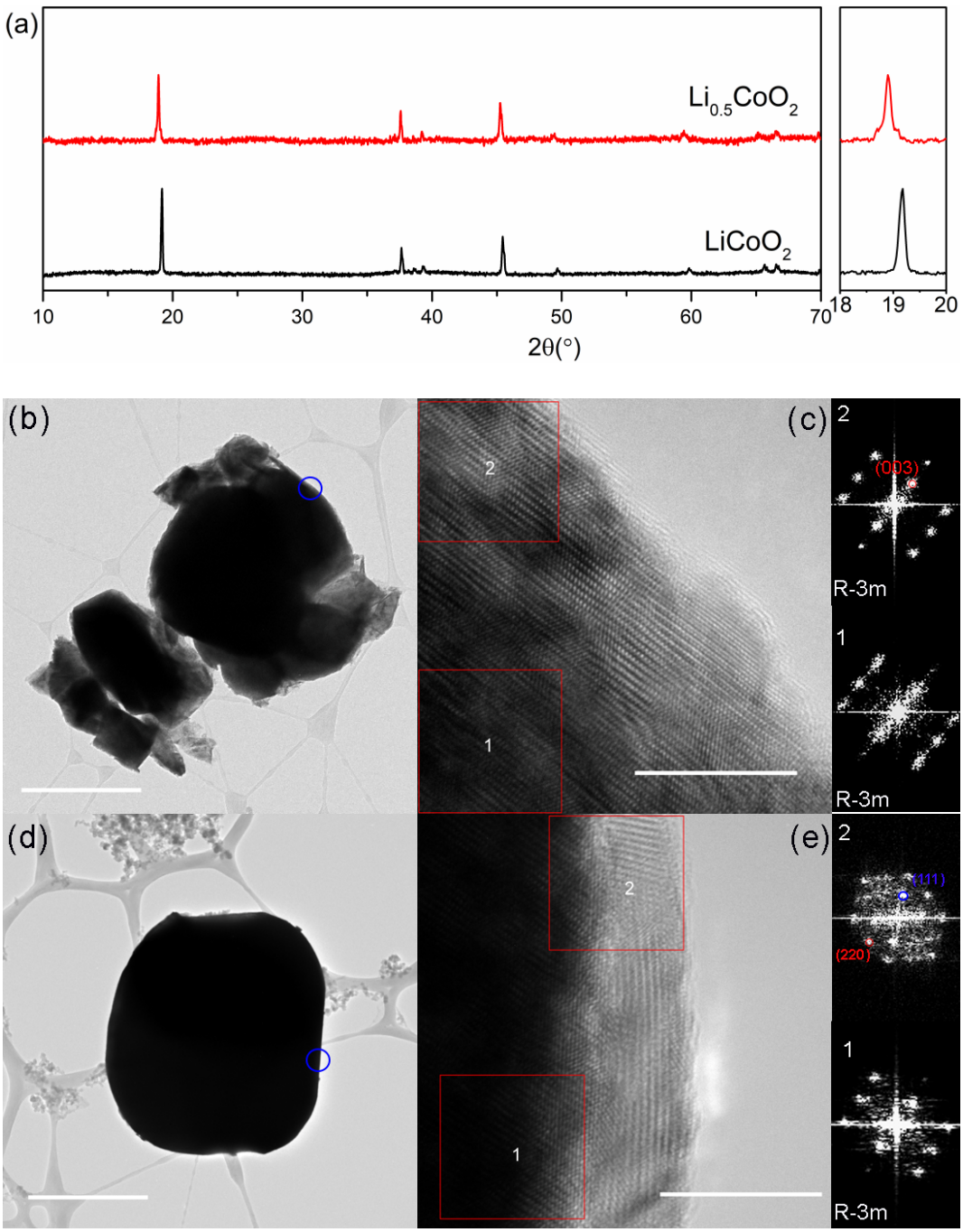

Supplementary Figure 37: (a) XRD pattern of chemical delithiation-derived $Li_{0.5}CoO_2$. TEM image of **(b)-(c)** pristine and **(d)-(e)** cycled $Li_{0.5}CoO_2$ (1 -1.6 V vs. RHE for 100 cycles) in 1 M KOH. The scale bar in **(b)-(e)** represents 1um, 10 nm, 2 um, and 10 nm, respectively.

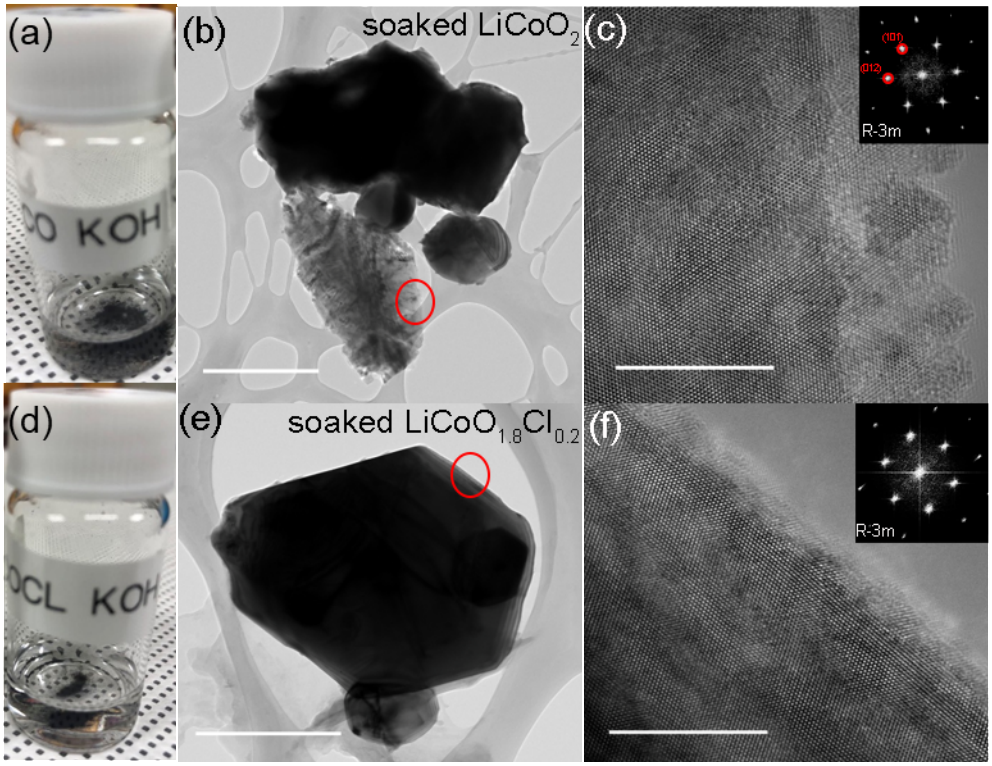

Supplementary Figure 38: Photo of **(a)** $LiCoO_2$ and **(d)** $LiCoO_{1.8}Cl_{0.2}$ after being soaked in 1 M KOH for 300 consecutive hours. Corresponding TEM images of soaked **(b)**, **(c)** $LiCoO_2$, and **(e)**, **(f)** $LiCoO_{1.8}Cl_{0.2}$. The scale bar in **(b)-(c)** and **(e)-(f)** represents 1um, 10 nm, 500 nm, and 10 nm, respectively.

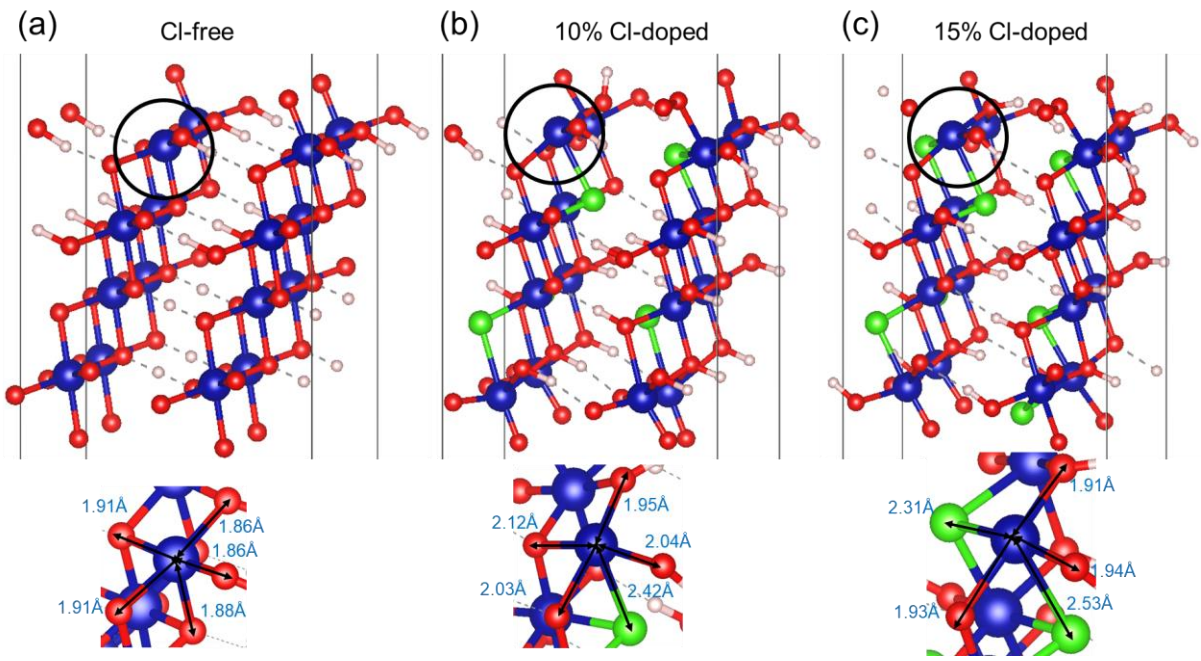

Supplementary Figure 39: DFT-optimized structures of (a) Cl-free, (b) 10% Cl-doped, and (c) 15% Cl-doped Co-oxyhydroxide surfaces, and local structure around the Co active centres (black circled) are shown in below. Color codes of the structures are blue, red, and green for Co, O, and Cl atoms, respectively.

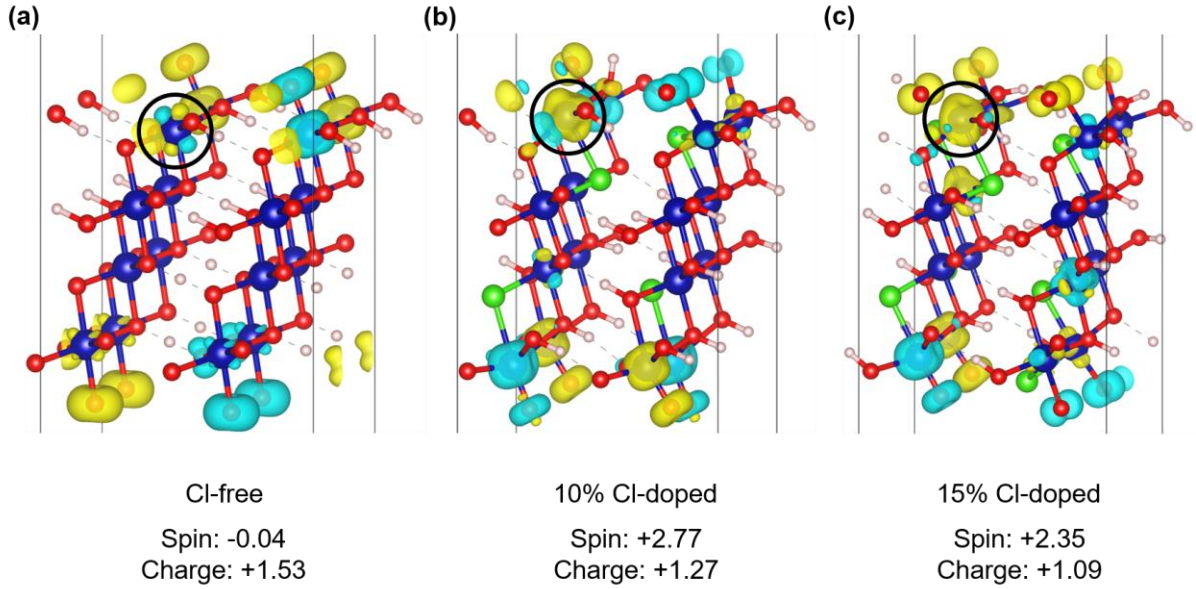

Supplementary Figure 40: Change of Bader charge and Bader spin of the Co active center (black circled) and spin density plots for (a) Cl-free, (b) 10% Cl-doped, and (c) 15% Cl-doped Co-oxyhydroxides. Color codes of the structures are blue, red, and green for Co, O, and Cl atoms, respectively. Iso-values was set as 0.02e/bohr^3 (yellow and cyan are for spin-up and spin-down electrons, respectively). Partial atomic spin and charge of the Co active center are calculated using Bader analysis, which are also displayed.

Supplementary Tables

Supplementary Table 1: Elemental contents derived from ICP and XPS

	Li (ppm)	Co (ppm)	Li : Co*	Cl♦ at.%
$LiCoO_2$	69025.71	602954.43	0.972	0
$LiCoO_{1.9}Cl_{0.1}$	72020.63	642818.17	0.951	3.01
$LiCoO_{1.8}Cl_{0.2}$	76930.11	635299.33	1.028	6.17

* obtained by ICP-MS; ♦ obtained by XPS

Supplementary Table 2. Refined structural parameters for $LiCoO_2$

$LiCoO_2$	x	y	z	Occupancy
Li	0	0	0.5	0.08333
Co	0	0	0	0.08333
O	0	0	0.25952	0.16667

Space group: R-3m.

Lattice parameter: a = b= 2.815 Å c =14.051 Å; $\alpha = \beta = 90.0^\circ$ $\gamma = 120.0^\circ$

$R_{expected}$ = 11.47 %, R_{Bragg} = 2.786, R_f = 1.545, χ^2 = 4.73

Supplementary Table 3. Refined structural parameters for $LiCoO_{1.9}Cl_{0.1}$

$LiCoO_{1.9}Cl_{0.1}$	x	y	z	Occupancy
Li	0	0	0.5	0.08333
Co	0	0	0	0.08333
O	0	0	0.26184	0.15251
Cl	0	0	0.26184	0.00814

Space group: R-3m.

Lattice parameter: a = b= 2.816 Å c =14.054 Å; $\alpha = \beta = 90.0^\circ$ $\gamma = 120.0^\circ$

$R_{expected}$ = 10.63 %, R_{Bragg} = 4.083, R_f = 2.918, χ^2 = 5.06

Supplementary Table 4. Refined structural parameters for $LiCoO_{1.8}Cl_{0.2}$

$LiCoO_{1.9}Cl_{0.1}$	x	y	z	Occupancy
Li	0	0	0.5	0.08333
Co	0	0	0	0.08333
O	0	0	0.25895	0.14778
Cl	0	0	0.25895	0.01406

Space group: R-3m.

Lattice parameter: a = b= 2.817 Å c =14.061 Å; $\alpha = \beta = 90.0^\circ$ $\gamma = 120.0^\circ$

$R_{expected}$ = 14.94 %, R_{Bragg} = 8.29, R_f = 5.62, χ^2 = 4.94

Supplementary Table 5. Structural parameters derived from a multiple shell fit in R space for the as-prepared samples.

Sample	Co-O			Co-Cl			Co-Co			ΔE_0	R
	N_{Co-O}	R(Å)	δ^2(Å)^2	N_{Co-Cl}	R(Å)	δ^2(Å)^2	N_{Co-Co}	R(Å)	δ^2(Å)^2		
$LiCoO_2$	6	1.90727	0.0020	/	/	/	6	2.83147	0.0028	-0.17	0.027
$LiCoO_{1.9}Cl_{0.1}$	5.28	1.90046	0.0008	0.33	1.94131	0.0008	5.36	2.82328	0.0025	-0.08	0.012
$LiCoO_{1.8}Cl_{0.2}$	4.58	1.90292	0.0015	0.50	2.09	0.0015	5.30	2.81614	0.0017	0.16	0.004

Supplementary Table 6. ECSA and BET comparison.

This study	ECSA (m^2/g)	BET (m^2/g)	Ratio (ECSA/BET)	**Ref**[7]	ECSA (m^2/g)	BET (m^2/g)	Ratio (ECSA/BET)
$LiCoO_2$	0.84	1.20	0.70	$LiCoO_2$	0.19	0.28	0.68
RuO_2	23.5	50.8	0.46	RuO_2	5.69	11.38	0.50
$LiCoO_{1.9}Cl_{0.1}$	1.04	2.11	0.49	/	/	/	/
$LiCoO_{1.8}Cl_{0.2}$	0.80	1.57	0.51	/	/	/	/

Supplementary Table 7. R_1 and R_2 estimated by fitting the equivalent circuit against the EIS.

	R_1 (Ω)	R_2 (Ω)
$LiCoO_2$	143	315
$LiCoO_{1.8}Cl_{0.2}$	8.0	15.8

Supplementary Table 8. OER activity comparison with the state-of-the-art catalysts.

Catalyst	Substrate	OER Activity	Test duration	Electrolyte	Source
$LiCoO_{1.8}Cl_{0.2}$	**Glassy carbon**	**200 mA mg_{oxide}^{-1}@1.52 V vs. RHE**	**durable within 500 h**	**1 M KOH**	**This work**
		50 mA cm_{geo}^{-2}@ 1.53 V vs. RHE			
		1 mA cm_{oxide}^{-2}@ 1.48 V vs. RHE			
		10 mA cm_{geo}^{-2}@ 1.50 V vs. RHE			
RuO_2	Glassy carbon	0.014 mA cm_{oxide}^{-2}@ 1.48 V vs. RHE	η increases by 12.5% in 10 h	1 M KOH	This work
$[Mn]_T[Al_{0.5}Mn_{1.5}]_OO_4$	Glassy carbon	1 mA cm_{oxide}^{-2}@ ~1.7 V vs. RHE	durable for 12 h	0.1 M KOH	Nat. Catal. 2020.[8]
$CoFe_{0.25}Al_{1.75}O_4$	Glassy carbon	10 mA cm_{geo}^{-2}@ ~1.54 V vs. RHE	η increases by ~3% in 48 h	1 M KOH	Nat. Catal. 2019.[9]
$Zn_{0.2}Co_{0.8}OOH$	Glassy carbon	50 mA cm_{geo}^{-2}@~1.50V vs. RHE	durable for 40 h	1 M KOH	Nat. Energy. 2019.[10]
w-$Ni(OH)_2$	Glassy carbon	80 mA cm_{geo}^{-2}@ 1.497V vs. RHE	durable for ~ 200 mins	1 M KOH	Nat. Commun.2019.[11]
PBA-60	Glassy carbon	10 mA cm_{geo}^{-2}@ 1.513 V vs. RHE	durable for 25 h	1 M KOH	Nat. Commun.2019.[12]
S|NiNx−PC/EG	N.A.	10 mA cm_{geo}^{-2}@ 1.51 V vs. RHE	durable for 10 h	1 M KOH	Nat. Commun.2019.[13]
$BiCoO_3$-$Bi_4Ti_3O_{12}$	Glassy carbon	10 mA cm_{geo}^{-2}@ 1.55 V vs. RHE	~87% current loss in 20 h	1 M KOH	Nat. Commun.2019.[14]
$CaCoO_3$	Glassy carbon	10 mA cm_{geo}^{-2}@ 1.49 V vs. RHE	~10% current loss in 20000 s	1 M KOH	Sci. Adv. 2019.[15]
$Co_3Sn_2S_2$	Ni foam	10 mA cm_{geo}^{-2}@ 1.53 V vs. RHE	durable for 12 h	1 M KOH	Sci. Adv.2019.[16]
NBCFM	Glassy carbon	10 mA cm_{geo}^{-2}@ 1.589 V vs. RHE	durable for 10 h	0.1 M KOH	Sci. Adv.2018.[17]
Fe–Co–P	Carbon paper	10 mA cm_{geo}^{-2}@ 1.499 V vs. RHE	durable for 100 h	1 M KOH	Energy. Environ. Sci. 2019.[18]
LCF-700	Glassy carbon	10 mA cm_{geo}^{-2}@ 1.523 V vs. RHE	durable for 100 h	0.1 M KOH	Energy. Environ. Sci. 2018.[19]
CoV-UAH	Glassy carbon	10 mA cm_{geo}^{-2}@ 1.48 V vs. RHE	durable for 170 h	1 M KOH	Energy. Environ. Sci. 2018.[20]
NCN-1000-5	Glassy carbon	10 mA cm_{geo}^{-2}@ 1.64 V vs. RHE	~12% current loss in 12000 s	0.1 M KOH	Energy. Environ. Sci. 2019.[21]
BSCF	Glassy carbon	10 mA mg_{oxide}^{-1}@1.55 V vs. RHE	durable for 500 cycles	0.1 M KOH	J. Am. Chem. Soc. 2019.[22]
C_{60}-SWCNT	Glassy carbon	10 mA cm_{geo}^{-2}@ 1.69 V vs. RHE	7.9 % current loss in 10 h	0.1 M KOH	J. Am. Chem. Soc. 2019.[23]
NSFLGDY-900	Glassy carbon	10 mA cm_{geo}^{-2}@ 1.529 V vs. RHE	5% current loss in 20000 s	0.1 M KOH	J. Am. Chem. Soc. 2019.[24]
NiCoFe@NiCoFeO NTAs	carbon fiber cloth	10 mA cm_{geo}^{-2}@ 1.43 V vs. RHE	durable for 12 h	1 M KOH	J. Am. Chem. Soc. 2019.[25]
a-LNF(t-d)	Ni foam	~360 mA mg_{oxide}^{-1}@1.53 V vs. RHE	durable for 100 h	1 M KOH	Adv. Mater. 2019.[26]
HCM@Ni-N	carbon fiber cloth	10 mA cm_{geo}^{-2}@ 1.534 V vs. RHE	η increases by 1.2 % in 12 h	1 M KOH	Adv. Mater. 2019.[27]
NiTe/NiS	Ni foam	100 mA cm_{geo}^{-2}@ 1.551 V vs. RHE	η increases by 6 % in 50 h	1 M KOH	Adv. Mater. 2019.[28]
A-Ni@G	Glassy carbon	10 mA cm_{geo}^{-2}@ 1.50V vs. RHE	durable for 10 h	1 M KOH	Chem.2018.[29]
$La_{0.5}Ba_{0.25}Sr_{0.25}CoO_{2.9-\delta}F_{0.1}$	Glassy carbon	100 mA cm_{geo}^{-2}@ 1.748 V vs. RHE	durable for 360 mins	1 M KOH	Chem. 2018.[30]
CTGU-10c2	Glassy carbon	10 mA cm_{geo}^{-2}@ 1.47V vs. RHE	durable for 50 h	0.1 M KOH	Angew. Chem. 2019.[31]
Co-Cu-W oxide	copper foam	10 mA cm_{geo}^{-2}@ 1.543V vs. RHE	durable for 10 h	0.1 M KOH	Angew. Chem. 2019.[32]
G-FeCoW	Glassy carbon	10 mA cm_{geo}^{-2}@ 1.453V vs. RHE	durable for 550 h	1 M KOH	Science. 2016.[33]
NiCo-UMOFNs	Glassy carbon	10 mA cm_{geo}^{-2}@ 1.48 V vs. RHE	2.6 % current loss in 200 h	1 M KOH	Nat. Energy. 2016.[34]
NiFe-LDH/CNT	Glassy carbon	2.5 mA cm_{geo}^{-2}@ ~1.46V vs. RHE	durable for 1000 s	1 M KOH	J.Am. Chem. Soc. 2013[35]

Note: the potential at a certain normalized current density by the disk area represents the OER activity of the catalyst-modified electrode. "Durable" means no obvious current density drop or overpotential increase at the end of the durability test.

The value of R for all fittings is less than 0.05, suggesting a good fit.[36] For the same sample at different potentials, the value of δ^2_{Co-Co} did not vary much from each other, suggesting the influence of Debye-Waller factor is limited. In addition, the derived δ^2_{Co-Co} is far less than 0.03 (Å)^2, implying a reliable fit with reasonable Debye-Waller factors.[37]

Supplementary Table 9. Fitting parameters of the Fourier-transformed k^3 -weighted Co K-edge EXAFS spectra of $LiCoO_2$ at different OER potentials.

Sample	Co-O			Co-Co			ΔE_0	R
	N_{Co-O}	R(Å)	δ^2(Å)^2	N_{Co-Co}	R(Å)	δ^2(Å)^2		
$LiCoO_2$@1.2V	5.88	1.90261	0.0009	6.26	2.81963	0.0013	-0.65	0.016
$LiCoO_2$@1.4V	5.89	1.90216	0.0008	6.38	2.81976	0.0014	-0.64	0.014
$LiCoO_2$@1.5V	5.90	1.90345	0.0009	6.30	2.81919	0.0013	-0.64	0.017
$LiCoO_2$@1.6V	5.96	1.89821	0.0009	6.38	2.82117	0.0013	-0.71	0.015

Supplementary Table 10. Fitting parameters of the Fourier-transformed k^3 -weighted Co K-edge EXAFS spectra of $LiCoO_{1.8}O_{0.2}$ at different OER potentials.

Sample	Co-O			Co-Co			ΔE_0	R
	N_{Co-O}	R(Å)	δ^2(Å)^2	N_{Co-Co}	R(Å)	δ^2(Å)^2		
$LiCoO_{1.8}Cl_{0.2}$@1.2V	4.55	1.90376	0.0020	5.39	2.82255	0.0029	-0.57	0.012
$LiCoO_{1.8}Cl_{0.2}$@1.4V	4.67	1.90305	0.0017	5.87	2.82766	0.0027	-0.13	0.006
$LiCoO_{1.8}Cl_{0.2}$@1.5V	5.02	1.91193	0.0023	6.20	2.83174	0.0026	0.38	0.018
$LiCoO_{1.8}Cl_{0.2}$@1.6V	5.02	1.91653	0.0015	6.64	2.84122	0.0034	0.56	0.030

Supplementary Table 11. DFT-calculated surface formation energies of oxyhydroxide structures ($CoO_{2-x}Cl_xH$), and spinel structures ($Co_3O_{4-2x}Cl_{2x}$ and $LiCo_2O_{4-2x}Cl_{2x}$). The unit is in J/m^2.

	Cl-free (x=0)		*Cl-doped (x=0.2)*	
	w/o solvation	w/ solvation	w/o solvation	w/ solvation
$CoO_{2-x}Cl_xH$ (0001) facet	1.22	1.06	1.96	1.77
$Co_3O_{4-2x}Cl_{2x}$ (111) facet	2.25	2.18	4.05	4.06
$LiCo_2O_{4-2x}Cl_{2x}$ (111) facet	0.83	0.46	2.75	2.05

Supplementary Note 1

Calculation of ECSA.

The electrochemical active surface area (ECSA) of the evaluated samples is calculated based on the following relationship:

$$\mathrm{ECSA} = \frac{C_{DL}}{C_s} \tag{1}$$

Where C_{DL} and C_s are the double-layer capacitance and specific capacitance, respectively. C_s = 0.10 mF cm^{-2} was chosen in 1 M KOH, according to previous reports.[7,38] Note that no conductive carbon support was used when testing the capacitive current of the metal oxides. Before the above scans, the studied materials have been pre-cycled in the potential region of 1.2 - 1.6 V vs. RHE until current density stabilized. C_{DL} is estimated from the CV current in a non-faradaic potential region, i.e., 1.0 - 1.1 V vs. RHE in this work:

$$\mathrm{i} = \dot{v}\ C_{DL} \tag{2}$$

In above equation, $\dot{v}$ is the potential scanning rate, and here 0.005 V s^{-1}, 0.01 V s^{-1}, 0.02 V s^{-1}, 0.05 V s^{-1}, 0.1 V s^{-1}, and 0.2 V s^{-1} are used. The CVs were collected without filtering.

Supplementary Note 2

Detecting the reaction product of the OER catalysis.

The differential electrochemical mass spectrometry (DEMS, Hiden analytical, HPR-40) was applied to examine the generated gas product during the OER catalyzed by $LiCoO_{1.8}Cl_{0.2}$. As shown in Supplementary Figure 16(a), the trend of generated O_2 (m/z =32) agreed well with the CV voltage profile. In addition, except the target O_2 gas, remaining H_2O moisture, N_2, and their sub-moieties, other impure gases/moieties (e.g., Cl with m/z = 35.5) could not be detected (Supplementary Figure 16(b)), suggesting no significant evolution of Cl-contained gases. In addition, the potential leaching of Cl^- into the electrolyte (KOH) was examined by $AgNO_3$ aqueous solution with excessive HNO_3. From Supplementary Figure 16(c), there was no obvious detection of any white precipitates (AgCl) after cycling $LiCoO_{1.8}Cl_{0.2}$ for 1000 CV cycles, implying no significant leaching of Cl into the electrolyte. Based on the above experiments, significant Cl evolution as the side reaction was precluded.

Supplementary Note 3

Assessing the OER Faradaic efficiency.

The Rotating ring-disk electrode (RRDE) setup (inset in Supplementary Figure 17)) was used to estimate the OER Faradaic efficiency under $LiCoO_{1.8}Cl_{0.2}$ catalysis. The potential at the disk electrode is swept over the OER potential window while the potential of Pt ring is set at a value for the oxygen reduction reaction (ORR) to happen. The Faradaic efficiency of the examined OER catalyst is defined as $I_{ring}/(I_{disk}*N)$, where I_{ring} and I_{disk} are the current at the ring and disc electrode, respectively, and N is the collection efficiency of the Pt ring. The potential of the Pt ring (V_{ring}) was set to 0.4 V vs. RHE to reduce the generated O_2 from the disk electrode. From Supplementary Figure 17, I_{ring} increases with the rise of I_{disk}, yielding a Faradaic efficiency larger than 93%. When the potential of the Pt ring was switched to 1.5 V vs. RHE, no obvious oxidative ring current (attributed to the oxidation of H_2O_2) was detected, suggesting that the large OER current density under $LiCoO_{1.8}Cl_{0.2}$ catalysis was mainly ascribed to the desired $4e^-$ pathway ($4OH^- \rightarrow O_2 + 2H_2O + 4e^-$) rather than the $2e^-$ peroxide formation ($2OH^- \rightarrow H_2O_2 + 2e^-$).[39]

Supplementary Note 4

Structural and compositional characterization of cycled $LiCoO_2$.

From the TEM images in Supplementary Figure 35 (a)-(c), well-defined lattice fringes on the surface are detected for the cycled $LiCoO_2$. The corresponding FFT (Supplementary Figure 35(d)) detect strong reflections (e.g., (111), (220), (311)) of an $Fd\bar{3}m$ spinel structure.[40,41] Also, the FFT intensity of (111) plane is much more intense than that of (200) plane, implying the surface takes the $LiCo_2O_4$-type rather than Co_3O_4-type spinel structure.[40,41] In addition, the XPS (Supplementary Figure 35(e)) detected Li remained on the surface of cycled $LiCoO_2$, suggesting the cubic spinel $Li_{1\pm x}Co_2O_4$ (x<1) phase. The XRD (Supplementary Figure 35(f)) was displayed with logarithmic y-axis to highlight the minor diffraction peaks. The most pronounced XRD difference between layered and spinel $Li_{1\pm x}CoO_2$ lies at 2θ = 36–40° and 64–68° regions (highlighted by the rectangular box). Three diffraction peaks ((101), (006), (012)) are existing within 2θ = 36–40°, for the layered structure, in contrast to the two diffraction peaks ((311) and (222)) for the spinel structure which share similar 2θ position to the (101) and (012) peak, respectively.[42] "(006) peak" present in the layered structure is absent in the spinel structure. Since lithium stoichiometry is undetermined, the exact peak position cannot be a proof of the existence of spinel. Instead, decrease in (006) peak can be s a fingerprint which distinguish spinel from layered oxide. From the logscale XRD patterns, we revealed that (006) decreased slightly (right panel of Supplementary Figure S35(f)) which originated from spinel

phase generation at the surface. The EXAFS (Supplementary S35(g)) was also added for the activated $LiCoO_2$. Layered $LiCoO_2$ and spinel $Li_{1\pm x}Co_2O_4$ share similar EXAFS peak positions for the Co-O and edge-shared Co-Co coordination. The difference between the two structures lies at the peak around 3.0 Å which corresponds to the corner-shared Co. The relative intensity of this feature peak in spinel $Li_xCo_2O_4$ is much lower than that of spinel Co_3O_4, as the spinel $Li_xCo_2O_4$ contains Li ions in the corner-shared site.[6] From Supplementary S35(g), the intensity of this feature peak (highlighted with black circle) increased, which might be attributed to the spinel phase formation.

Supplementary Note 5

Investigation of surface restructuring for pre-delithiated $LiCoO_2$.

In order to investigate the effect of Li deficiency, a chemical delithiation method was applied to extract Li from layered $LiCoO_2$.[43] Briefly, the mixture of $LiCoO_2$ and the oxidizer NO_2BF_4 (>96% purity, Alfa Aesar) was stirred in an acetonitrile solution in an argon-filled glovebox. By controlling the stoichiometry between $LiCoO_2$ and NO_2BF_4 ($LiCO_2 + {}_xNO_2BF_4 \rightarrow Li_{1-x}CoO_2 + {}_xNO_2 + {}_xLiBF4$), $Li_{1-x}CoO_2$ with different Li deficiency (x) can be generated. To avoid the phase change, x in $Li_{1-x}CoO_2$ should not exceed 0.5.[43] As a result, we prepared $Li_{0.5}CoO_2$, whose layered lattice structure (R-3m) has been checked with XRD (Supplementary Figure 37(a)), and the atomic ratio of Li vs Co was confirmed by ICP-MS. From Supplementary Figure 37(c), the surface (region 2) and internal bulk (region 1) of pristine $Li_{0.5}CoO_2$ have similar structures with visually identical FFT pattern, which can be well indexed to its layered structure (R-3m). After cycling $Li_{0.5}CoO_2$ within 1 -1.6 V vs. RHE for 100 cycles, its surface (region 2 in Supplementary Figure 37(e)) restructured. The corresponding FFT detect strong reflections of an $Fd\bar{3}m$ spinel structure, e.g., (111) and (220) highlighted with blue and red circle, respectively. This suggests the formation of a $Li_{1\pm x}Co_2O_4$-type spinel phase.[40,41]

Supplementary Note 6

Calculation of surface formation energies.

In Figures 6(c) and 6(d) in the main text, we assessed the restructuring energetics using the bulk phase calculations, where neither a facet nor a solvation effect is present. This is reasonable because the surface reconstruction region observed in the experiment is tens-of-nanometer thick (corresponding to a few tens of layers, at least), and hence the contribution of the surface effect is expected to be marginal. For a complete understanding, we further calculated the surface formation energies, ΔE_{surf} of oxyhydroxide structures and spinel structures. We chose stable low-index facets, which are considered to predominantly exist on the surface,[44,45] and also considered the solvation effect using an implicit solvation model as implemented in the VASPsol.[46] As shown in Supplementary Table 11, the solvation cannot change the trend in ΔE_{surf}, although it slightly helps to stabilize the surface formation. Moreover, ΔE_{surf} of the Li-free spinel structure ($Co_3O_{4-2x}Cl_{2x}$) is relatively larger than ΔE_{surf} of the others, implying that the unlikely formation of Li-free spinel structure at the surface. Most interestingly, the Cl-doping dramatically decreases ΔE_{surf} of the oxyhydroxide over the lithium-containing spinel structure, yielding ΔE_{surf} ($CoO_{1.8}Cl_{0.2}H$) < ΔE_{surf} ($LiCo_2O_{3.6}Cl_{0.4}$) that is in stark contrast to the Cl-free case; ΔE_{surf} (CoOOH) > ΔE_{surf} ($LiCo_2O_4$). Thus, we conclude that the surface effect also favors the formation of the lithium-containing spinel structure for the Cl-free case and the formation of oxyhydroxide structure for the Cl-doped case.

Supplementary Note 7

The HO/O/HOO binding energy with different Cl contents.

We note that the binding energies of HO/O/HOO with Cl appear nonmonotonic in our calculation (i.e. the binding energy at 15% Cl is in between that at 0% and 10% of Cl). This may be attributed to two competing effects of Cl with varying doping concentrations. First, Cl coordination distorts the local symmetry near the Co center and downshifts the part of Eg levels (i.e. distortion effect), which serve as accepting states for HO/O/HOO binding (Supplementary Figure 39 about local structure). Second, as the electronegativity of Cl is lower than O, it pushes an electron density to the metal center and upshifts the accepting states (i.e. induction effect). Once Cl is doped even at a low level (e.g. 10%), the distortion effect appears, which reduces the Co^{3+} to Co^{2+}, and increases the intermediate binding energies. As Cl doping level further increases to 15%, the induction effect subtly decreases the intermediate binding energy to the Co^{2+}. Indeed, the atomic spin/charge of the Co center (Supplementary Figure 39 and 40 about the Bader spin/charge analyses) from the Bader analyses supports that the valence of the Co center is changed to 2^{+} at 10% of Cl (partial spin of the Co dramatically changes from 0 to 2.3), and then inductively acquires more electron density at 15% of Cl (partial charge of the Co decreases from 1.27 to 1.09) while its local spin moment remain nearly untouched.

Supplementary References:

1 Nishi, T., Nakai, H. & Kita, A. Visualization of the state-of-charge distribution in a LiCoO2 cathode by in situ Raman imaging. *Journal of The Electrochemical Society* **160**, A1785-A1788, (2013).

2 Liao, L. *et al.* A nanoporous molybdenum carbide nanowire as an electrocatalyst for hydrogen evolution reaction. *Energy & Environmental Science* **7**, 387-392, (2014).

3 Shervedani, R. K. & Madram, A. R. Kinetics of hydrogen evolution reaction on nanocrystalline electrodeposited Ni62Fe35C3 cathode in alkaline solution by electrochemical impedance spectroscopy. *Electrochimica Acta* **53**, 426-433, (2007).

4 Cao, L. *et al.* Identification of single-atom active sites in carbon-based cobalt catalysts during electrocatalytic hydrogen evolution. *Nature Catalysis* **2**, 134-141, (2019).

5 Bergmann, A. *et al.* Unified structural motifs of the catalytically active state of Co(oxyhydr)oxides during the electrochemical oxygen evolution reaction. *Nature Catalysis* **1**, 711-719, (2018).

6 Kim, Y., Hong, Y., Ryu, K. S., Kim, M. G. & Cho, J. Structural changes of bare and AlPO4-coated LixCoO2 (x= 0.24 and 0.1) upon thermal annealing≥ 200° C. *Journal of Power Sources* **179**, 780-784, (2008).

7 Jung, S., McCrory, C. C., Ferrer, I. M., Peters, J. C. & Jaramillo, T. F. Benchmarking nanoparticulate metal oxide electrocatalysts for the alkaline water oxidation reaction. *Journal of Materials Chemistry A* **4**, 3068-3076, (2016).

8 Sun, Y. *et al.* Covalency competition dominates the water oxidation structure–activity relationship on spinel oxides. *Nature Catalysis*, (2020).

9 Wu, T. *et al.* Iron-facilitated dynamic active-site generation on spinel CoAl2O4 with self-termination of surface reconstruction for water oxidation. *Nature Catalysis*, (2019).

10 Huang, Z.-F. *et al.* Chemical and structural origin of lattice oxygen oxidation in Co–Zn oxyhydroxide oxygen evolution electrocatalysts. *Nature Energy* **4**, 329-338, (2019).

11 Yan, J. *et al.* Single atom tungsten doped ultrathin α-Ni(OH)2 for enhanced electrocatalytic water oxidation. *Nature Communications* **10**, 2149, (2019).

12 Yu, Z.-Y. *et al.* Unconventional CN vacancies suppress iron-leaching in Prussian blue analogue pre-catalyst for boosted oxygen evolution catalysis. *Nature Communications* **10**, 2799, (2019).

13 Hou, Y. *et al.* Atomically dispersed nickel–nitrogen–sulfur species anchored on porous carbon nanosheets for efficient water oxidation. *Nature Communications* **10**, 1392, (2019).

14 Li, X. *et al.* Enhancing oxygen evolution efficiency of multiferroic oxides by spintronic and ferroelectric polarization regulation. *Nature Communications* **10**, 1409, (2019).

15 Li, X. *et al.* Exceptional oxygen evolution reactivities on CaCoO₃ and

SrCoO₃. *Science Advances* **5**, eaav6262, (2019).

16 Li, G. *et al.* Surface states in bulk single crystal of topological semimetal Co₃Sn₂S₂ toward water oxidation. *Science Advances* **5**, eaaw9867, (2019).

17 Kim, N.-I. *et al.* Oxygen-deficient triple perovskites as highly active and durable bifunctional electrocatalysts for oxygen electrode reactions. *Science Advances* **4**, eaap9360, (2018).

18 Zhang, H., Zhou, W., Dong, J., Lu, X. F. & Lou, X. W. Intramolecular electronic coupling in porous iron cobalt (oxy)phosphide nanoboxes enhances the electrocatalytic activity for oxygen evolution. *Energy & Environmental Science*, (2019).

19 Song, S. *et al.* Operando X-ray spectroscopic tracking of self-reconstruction for anchored nanoparticles as high-performance electrocatalysts towards oxygen evolution. *Energy & Environmental Science* **11**, 2945-2953, (2018).

20 Liu, J. *et al.* Ultrathin amorphous cobalt–vanadium hydr(oxy)oxide catalysts for the oxygen evolution reaction. *Energy & Environmental Science* **11**, 1736-1741, (2018).

21 Jiang, H. *et al.* Defect-rich and ultrathin N doped carbon nanosheets as advanced trifunctional metal-free electrocatalysts for the ORR, OER and HER. *Energy & Environmental Science* **12**, 322-333, (2019).

22 Kim, B.-J. *et al.* Functional Role of Fe-Doping in Co-Based Perovskite Oxide Catalysts for Oxygen Evolution Reaction. *Journal of the American Chemical Society* **141**, 5231-5240, (2019).

23 Gao, R., Dai, Q., Du, F., Yan, D. & Dai, L. C60-Adsorbed Single-Walled Carbon Nanotubes as Metal-Free, pH-Universal, and Multifunctional Catalysts for Oxygen Reduction, Oxygen Evolution, and Hydrogen Evolution. *Journal of the American Chemical Society* **141**, 11658-11666, (2019).

24 Zhao, Y. *et al.* Stereodefined Codoping of sp-N and S Atoms in Few-Layer Graphdiyne for Oxygen Evolution Reaction. *Journal of the American Chemical Society* **141**, 7240-7244, (2019).

25 Liu, Y. *et al.* Valence Engineering via Selective Atomic Substitution on Tetrahedral Sites in Spinel Oxide for Highly Enhanced Oxygen Evolution Catalysis. *Journal of the American Chemical Society* **141**, 8136-8145, (2019).

26 Chen, G. *et al.* An Amorphous Nickel–Iron-Based Electrocatalyst with Unusual Local Structures for Ultrafast Oxygen Evolution Reaction. *Advanced Materials* **31**, 1900883, (2019).

27 Zhang, H. *et al.* Unveiling the Activity Origin of Electrocatalytic Oxygen Evolution over Isolated Ni Atoms Supported on a N-Doped Carbon Matrix. *Advanced Materials* **0**, 1904548.

28 Xue, Z. *et al.* Interfacial Electronic Structure Modulation of NiTe Nanoarrays with NiS

Nanodots Facilitates Electrocatalytic Oxygen Evolution. *Advanced Materials* **31**, 1900430, (2019).

29 Zhang, L. *et al.* Graphene Defects Trap Atomic Ni Species for Hydrogen and Oxygen Evolution Reactions. *Chem* **4**, 285-297, (2018).

30 Hua, B. *et al.* Activating p-blocking centers in perovskite for efficient water splitting. *Chem* **4**, 2902-2916, (2018).

31 Zhou, W. *et al.* Stable Hierarchical Bimetal–Organic Nanostructures as HighPerformance Electrocatalysts for the Oxygen Evolution Reaction. *Angewandte Chemie International Edition* **58**, 4227-4231, (2019).

32 Gao, D. *et al.* Modular Design of Noble-Metal-Free Mixed Metal Oxide Electrocatalysts for Complete Water Splitting. *Angewandte Chemie International Edition* **58**, 4644-4648, (2019).

33 Zhang, B. *et al.* Homogeneously dispersed multimetal oxygen-evolving catalysts. *Science* **352**, 333-337, (2016).

34 Zhao, S. *et al.* Ultrathin metal–organic framework nanosheets for electrocatalytic oxygen evolution. *Nature Energy* **1**, 16184, (2016).

35 Gong, M. *et al.* An advanced Ni–Fe layered double hydroxide electrocatalyst for water oxidation. *Journal of the American Chemical Society* **135**, 8452-8455, (2013).

36 Kelly, S., Hesterberg, D. & Ravel, B. Analysis of soils and minerals using X-ray absorption spectroscopy. *Methods of Soil Analysis Part 5—Mineralogical Methods* **5**, 387-463, (2008).

37 Calvin, S. *XAFS for Everyone*. (CRC press, 2013).

38 McCrory, C. C., Jung, S., Peters, J. C. & Jaramillo, T. F. Benchmarking heterogeneous electrocatalysts for the oxygen evolution reaction. *Journal of the American Chemical Society* **135**, 16977-16987, (2013).

39 McCrory, C. C. L., Jung, S., Peters, J. C. & Jaramillo, T. F. Benchmarking Heterogeneous Electrocatalysts for the Oxygen Evolution Reaction. *Journal of the American Chemical Society* **135**, 16977-16987, (2013).

40 Gardner, G. *et al.* Structural basis for differing electrocatalytic water oxidation by the cubic, layered and spinel forms of lithium cobalt oxides. *Energy & Environmental Science* **9**, 184-192, (2016).

41 Lee, S. W. *et al.* The nature of lithium battery materials under oxygen evolution reaction conditions. *Journal of the American Chemical Society* **134**, 16959-16962, (2012).

42 Maiyalagan, T., Jarvis, K. A., Therese, S., Ferreira, P. J. & Manthiram, A. Spinel-type lithium cobalt oxide as a bifunctional electrocatalyst for the oxygen evolution and oxygen reduction reactions. *Nature Communications* **5**, 3949, (2014).

43 Venkatraman, S. & Manthiram, A. Synthesis and Characterization of P3-Type CoO2-δ.

Chemistry of Materials **14**, 3907-3912, (2002).

44 Bajdich, M., García-Mota, M., Vojvodic, A., Nørskov, J. K. & Bell, A. T. Theoretical Investigation of the Activity of Cobalt Oxides for the Electrochemical Oxidation of Water. *Journal of the American Chemical Society* **135**, 13521-13530, (2013).

45 Su, D., Dou, S. & Wang, G. Single Crystalline Co3O4 Nanocrystals Exposed with Different Crystal Planes for Li-O2 Batteries. *Scientific reports* **4**, 5767, (2014).

46 Mathew, K., Sundararaman, R., Letchworth-Weaver, K., Arias, T. & Hennig, R. G. Implicit solvation model for density-functional study of nanocrystal surfaces and reaction pathways. *The Journal of Chemical Physics* **140**, 084106, (2014).